IDEA League

Master of Science in Applied Geophysics

Research Thesis

From Seismology to Bridge Monitoring: Coda Wave Interferometry

Niklas Epple

August 8, 2018

TU Delft ETH Zurich RWTH Aachen

From Seismology to Bridge Monitoring: Coda Wave Interferometry

Master of Science Thesis

for the degree of Master of Science in Applied Geophysics at
Delft University of Technology
ETH Zürich
RWTH Aachen University
by

Niklas Epple

August 8, 2018

Department of Geoscience & Engineering · Delft University of Technology
Department of Earth Sciences · ETH Zürich
Faculty of Georesources and Material Engineering · RWTH Aachen University

Printed in Germany

IDEA LEAGUE
JOINT MASTER'S IN APPLIED GEOPHYSICS

Delft University of Technology, The Netherlands
ETH Zürich, Switzerland
RWTH Aachen, Germany

Dated: *August 8, 2018*

Committee Members:

Dr. rer. nat. Ernst Niederleithinger (RWTH Aachen)

Dr. Dirk-Jan van Manen (ETH Zürich)

Supervisor(s): Dr. rer. nat. Ernst Niederleithinger

Eidesstattliche Versicherung

Epple, Niklas — 374392

Name, Vorname — Matrikelnummer (freiwillige Angabe)

Ich versichere hiermit an Eides Statt, dass ich die vorliegende Arbeit/Bachelorarbeit/ Masterarbeit* mit dem Titel

From Seismology to Bridge Monitoring:
Coda Wave Interferometry

selbständig und ohne unzulässige fremde Hilfe erbracht habe. Ich habe keine anderen als die angegebenen Quellen und Hilfsmittel benutzt. Für den Fall, dass die Arbeit zusätzlich auf einem Datenträger eingereicht wird, erkläre ich, dass die schriftliche und die elektronische Form vollständig übereinstimmen. Die Arbeit hat in gleicher oder ähnlicher Form noch keiner Prüfungsbehörde vorgelegen.

Ort, Datum — Unterschrift

*Nichtzutreffendes bitte streichen

Belehrung:

§ 156 StGB: Falsche Versicherung an Eides Statt

Wer vor einer zur Abnahme einer Versicherung an Eides Statt zuständigen Behörde eine solche Versicherung falsch abgibt oder unter Berufung auf eine solche Versicherung falsch aussagt, wird mit Freiheitsstrafe bis zu drei Jahren oder mit Geldstrafe bestraft.

§ 161 StGB: Fahrlässiger Falscheid; fahrlässige falsche Versicherung an Eides Statt

(1) Wenn eine der in den §§ 154 bis 156 bezeichneten Handlungen aus Fahrlässigkeit begangen worden ist, so tritt Freiheitsstrafe bis zu einem Jahr oder Geldstrafe ein.

(2) Straflosigkeit tritt ein, wenn der Täter die falsche Angabe rechtzeitig berichtigt. Die Vorschriften des § 158 Abs. 2 und 3 gelten entsprechend.

Die vorstehende Belehrung habe ich zur Kenntnis genommen:

Ort, Datum — Unterschrift

Abstract

Concrete is the most widely used building material in the world and its stability assessment is of utmost importance for society. Ultrasonic measurements are one tool for investigation of concrete stability. The goal of those measurements is the derivation of damage sensitive parameters. The way ultrasound diffuses through concrete is affected by cracks in the specimen, so the description of diffusion can show potential damage indicators. Furthermore, the velocity of the wave propagation changes in damaged specimen. With the analysis of the late part of the seismic signal, small velocity changes can be detected and possibly linked to damage. When concrete is loaded, stress and strain change. This is linked non-linearly to velocity changes with the acoustoelastic theory, defining classical and non-classical non-linear parameters as possible damage indicators. In this work, the aforementioned methods and measures are applied to data from loading experiments on specimen of the size and structure of reinforced bridge girders. Ultrasound measurements with embedded sensors, as well as strain measurements were conducted until the girder failed. The analysis shows, that, while the diffusion of ultrasound can be approximated and parameters can be extracted, those parameters are only damage sensitive to some extent and at stages the specimen already shows damages. The velocity changes calculated with coda wave interferometry show a better response when damages appear and local anomalies give information about the location of damaged and extensively strained areas. A link between strain and velocity change shows that the non-linear relation between both measurements can be approximated with a second order polynomial according to the acousto-elastic effect. The parameters of this polynomial are the classical non-linear parameters and accord with literature values. A combination of all three applied methods shows good potential for the setup of a monitoring framework.

Acknowledgements

First of all I want to thank my supervisor Dr. Ernst Niederleithinger for the support during my thesis project. His door was always open for questions and discussions, even in busy times and on short notice. Special thanks go to all people of BAM department 8.2, especially to the division secretary Larina Karger and my roommates Kerstin Borchardt-Giers and Jens Wöstmann which helped me trough the bureaucratic jungle of BAM and assisted whenever help was needed. I would also like to thank Martin Herbrand for assisting me with the interpretation and analysis of the RWTH Aachen dataset, as well as all other people who provided me with valuable information on the project. Last but not least I would like to thank my family and friends for the support they gave me during the research period.

RWTH Aachen University
August 8, 2018

Niklas Epple

Table of Contents

List of Figures

List of Tables

Nomenclature

Latin Symbols

$\mathbf{u}$	Displacement vector
t	Time [s]
v, V	Velocity [m/s]
K	Bulk modulus [Pa]
E	Young's modulus [Pa]
f	Frequency [Hz]
l	Scattering mean free path [m]
l_*	Transport mean free path [m]
E_p, E_s	P-/S-wave energy [J]
$E(\mathbf{r}, t, f)$	Spectral energy density
$\mathbf{r}$	Distance vector [m]
D	Diffusivity [m^2/s]
$S(\mathbf{r}, t, f)$	Source term
P_0	Source pulse intensity
d	Number of dimensions
r	Distance [m]
u_u, u_{pt}	(Un)Perturbed wavefield
$A_T(t)$	Wave amplitude
C	Stiffness tensor
k, l, m	Murnaghan parameters

Greek Symbols

ρ	Density [kg/m^3]
λ	Lamè's first parameter (λ is also used as wavelength in the context of wave scattering)

μ	Lamè's second parameter
∇	Nabla operator
σ	Stress [Pa] (in the context of diffusion, σ is the dissipation rate)
Ω	Solution space
τ	Time shift
α	Stretching factor (in the context of the acoustoelastic theory, alpha is the non-classical non-linear parameter)
ϵ	Strain
ν	Poisson ratio
β	Quadratic nonlinear parameter
δ	Cubic nonlinear parameter

Subscripts

$_p$	Corresponding to P-wave
$_s$	Corresponding to S-wave
$_u$	Unperturbed
$_{pt}$	Perturbed

Other

[Pa/MPa]	Pascal/Megapascal
[Hz/kHz]	Hertz/Kilohertz
C30/37	Concrete specification according to DIN EN 206-1/Din 1045-2
°, [deg]	Degrees
D#D	Concrete strain gauge
R#D/H/V	Inductive displacement sensor
S07E08	Source-receiver combination 07-08

Acronyms

BAM Bundesanstalt für Materialforschung und -prüfung

BASt Bundesanstalt für Straßenwesen

CC Correlation Coefficient

CWI Coda Wave Interferometry

DCI Digital Image Correlation

NDT Non-Destructive Testing

NMR Nuclear Magnetic Resonance

P-Wave Compressional-wave

RWTH Rheinisch-Westfälische Technische Hochschule

S-Wave Shear-wave

SNR Signal to Noise Ratio

TOF Time Of Flight

US Ultrasound

Chapter 1

Introduction

Concrete is globally used to build houses, bridges and many other types of constructions. It can be used as a containment layer for nuclear power plants or castor containers, as well as a safety barrier for impact protection from accidents or terrorist attacks. This wide spread range of applications has made concrete the main construction material (Neroth, 2011).

The stability of concrete structures must be ensured during a building's lifespan due to their utmost importance for infrastructure and society. Therefore, it is important to check and monitor the stability of the concrete from time to time, to detect cracks or corrosion early enough to prevent failure and start repair work. On the surface, cracks in concrete can be found by visual inspection. To validate the presence of inner damage in a concrete structure the only method giving a true result is the investigation of a drilling core in the area of suspected damage. Although giving a reliable result, this method requires a reasonable suspicion of damage in this area and is not suitable for assessment and inspection. Therefore it is important to have on site testing methods covering large areas, while not damaging the structure. This field of civil engineering is called Non-Destructive Testing (NDT). Several methods well known in geophysics have made their way into NDT. Georadar, Nuclear Magnetic Resonance (NMR) and seismic (mainly ultrasonic) measurements are the most prominent of those. While Georadar and NMR are mainly on site testing methods, seismic measurements also bear a great potential for monitoring with embedded or permanently attached sensors.

Monitoring concrete structures, especially those exposed to strong loading or frequently changing environmental parameters, like bridges, with ultrasound (US) is a field of ongoing research in NDT. While for already built structures the ultrasound transducers are attached to the outside of the structure in general, which may introduce coupling problems, strong influence by environmental parameters and possible destruction by vandalism, it is possible to embed US-sensors directly into the concrete during (and also after) construction. The layout of the sensors can be designed individually for every structure to create a perfectly suited monitoring framework. Modern data transmission technologies make it possible to send the recorded data to a monitoring center.

The main technique for analysis of ultrasound measurements in concrete is the *Time Of Flight* (TOF) analysis to detect velocity changes. As small velocity changes can hardly be

detected by the TOF analysis, in recent years the so called *Coda Wave Interferometry* (CWI) has been adapted from Geophysics. Coda wave interferometry calculates velocity changes between different measurements. These velocity changes can be an indicator for a change in the structure, but an exact determination of different damages and a localization is difficult and part of ongoing research (Planès and Larose, 2013).

In this thesis, US measurements taken with embedded sensors at different bridge girders in loading experiments will be analysed. The bridge girders were made of reinforced, prestressed concrete and loaded stepwise until complete failure. For NDT it is necessary to evaluate the measurements for parameters providing relevant *in situ* information (Payan et al., 2010). Therefore, the experimental data is analysed in order to test different parameters reported in literature as possible damage indicators.

With the assessment of the different possible parameters I aim to provide information for the future development of monitoring strategies in bridges and other concrete structures. One significant question is whether laboratory experiments, specifically designed for the extraction of one parameter, are scalable and applicable in the framework of a complex concrete structure. The provided dataset should mimic the situation of a real-sized monitoring task. Therefore, it is used as a testing dataset for various applications of ultrasound processing techniques. It has already been processed and analysed with CWI (as published in Niederleithinger et al. (2018)). These calculated velocity changes will be further analysed as a first possible damage indicator.

As the propagation of ultrasound through a strongly scattering medium like concrete can be regarded as diffusive, the diffusion of the wave through concrete is another aspect the measurements can be analysed for. A parameter describing the diffusivity can therefore also be a damage indicator as cracks in a medium change wave diffusion in the concrete. Studies about diffusivity in concrete have already been done so a comparison of the results of this larger scale experiment to small scale experiments for validation is possible (see Ramamoorthy et al. (2004), Deroo et al. (2010), Fröjd (2018)).

During the loading experiment not only ultrasonic measurements were conducted. Aachen University (*Rheinisch-Westfälische Technische Hochschule (RWTH)*) also measured strains in and on the concrete as well as deflection. In an early stage of loading, concrete is known to deform elastically and stresses and strains to be linearly dependant. Therefore, I will attempt to recognize relations between strain and CWI velocity changes in the elastic deformation phase. This can be used for monitoring, where one assumes mainly undamaged concrete and elastic deformation. When the stress-strain relation becomes nonlinear at a certain load, but deformations are still elastic, the acoustoelastic effect links sound velocity changes to changes in the stress/strain field of a solid body. Therefore, a combination of strain measurements and ultrasonic measurements bears potential for the extraction of further nonlinear damage indicators with the help of the acoustoelastic theory. The determination of non-linear parameters from US measurements in concrete is a major topic of ongoing research in CWI, as these parameters are assumed to be applicable to a large damage range (Payan et al., 2010).

The following thesis will start with a description of the methods used with the corresponding theory. Afterwards, measurement data from the aforementioned experiment will be analysed and the results will be discussed in light of current literature to asses the applicability of the used methods in an experiment of such kind. In the end, possibilities for future work with this dataset as well as suggestions for further experiments on the studied topics will be made.

Chapter 2

Theory and Methods

This chapter will introduce the methodology used for the analysis of the ultrasound measurements and provide physical and mathematical background to these methods, as well as to the behaviour of concrete structures under load. The example figures given in this chapter are, unless otherwise noted, based on a synthetic dataset.

2.1 Concrete as Construction Material

Concrete is by far the most important construction material in the world. According to Neroth (2011, Chapter 3), more than 50% of all constructions are made of concrete. Concrete in general is a mixture of a paste consisting of water and cement and aggregates, which can for example be gravel or sand. According to the *Portland Cement Association* it generally contains:

- up to 8% of air
- $7\% - 15\%$ of cement
- $14\% - 21\%$ of water
- $60\% - 75\%$ of aggregates

The mixture of those components is adjusted to the specific requirements. While normal concrete, for example for bridge construction, needs to be very pressure resistant, one might also require the concrete to function as an insulation material and therefore contain larger pores (Neroth, 2011, Chapter 3).

Concrete itself is characterized by a high level of compressive strength but lacks in tensile strength. It will only reach between $5\% - 15\%$ tensile strength compared to its compressive strength. Therefore, it is often reinforced by steel to combine the high compressive strength

of concrete with the high tensile strength of steel (Zilch and Zehetmaier, 2006, Chapter 3). This is important, as there will always be a mixture of compressional and shear forces.

When concrete is loaded it will follow the typical stress-strain relation in the beginning, until the material fails (Zilch and Zehetmaier, 2006, Chapter 3). The stress-strain relation will be further discussed in section 2.5.

2.2 Acoustic Waves

It is well known that there are two general types of acoustic waves propagating through media, namely compressional waves (or P-waves) and shear waves (S-waves). For P-waves, particles move in the direction of the wave, for S-waves, the particle displacement is perpendicular to the wave direction. P- and S-waves have different material dependent propagation speeds, where P-waves are always faster than S-waves. In inhomogeneous (e.g. layered) and finite media, acoustic waves will be reflected at boundaries, layers and disturbances or scattered in many directions. In Geophysics, reflections at boundaries can be used for a systematic exploration of the subsurface. Under special conditions, there are also so called surface waves propagating along the surface of a medium. These waves can only develop along the free surface, where there is a transition from a solid to air (or water) and can appear in different modes like Love and Rayleigh waves, for example. Surface waves are always slower than the P- and S-waves but, as especially Rayleigh waves are the most destructive wave-type which develops during an earthquake, very important for seismology.

2.2.1 Coda

Looking at the record of seismic waves (in this case an earthquake recording), as displayed in figure 2.1 one can see the different wavemodes, the P-, S- and Rayleigh waves and the coda, which includes surface waves as well. Aki (1969) suggested that the coda part of a seismic record is the result of backscattering of numerous randomly distributed heterogeneities in the earth, which he proved in his later work. The coda has travelled longer distances through the material than the direct ballistic waves and covered a larger area. As it is a combination of multiple paths and includes several scattering events, it is difficult or almost impossible to get any directional information from the coda. Nevertheless, there is information hidden within the coda, as e.g. Rayleigh and Love waves are often in the noisy last part of a seismic recording. For instance, Stehly et al. (2008) show that they are able to reconstruct the greens function, using correlation of coda parts of seismic recordings to retrieve Love and Rayleigh modes. In this thesis, the fact will be used that the coda waves have spent more time in the medium and sensed a larger area before being recorded in order to analyse small velocity changes, which would be undetectable in the first arrival.

2.2.2 Ultrasound

Acoustic waves of frequencies above the upper limit of human hearing (approximately $>$ 20.000 Hz) are commonly referred to as ultrasound. Acoustic sources used for geophysical exploration are generally low frequencies up to 200 Hz and therefore located around the lower

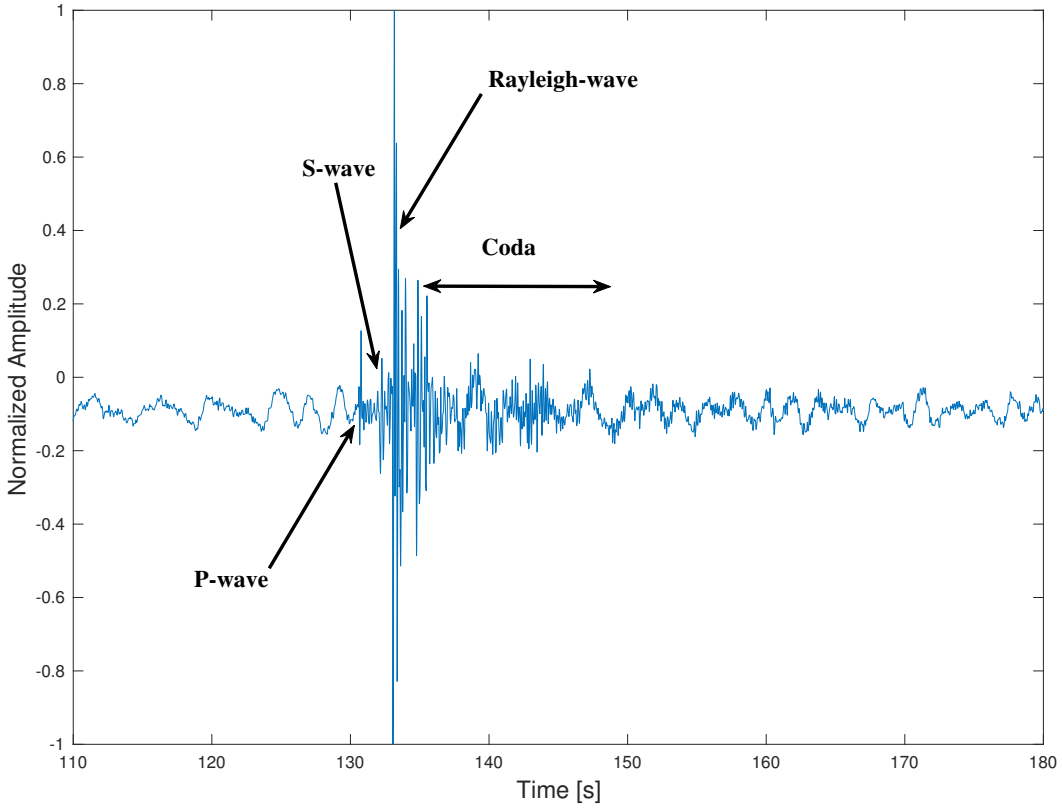

Figure 2.1: This sample recording of an earthquake from the German upper Vogtland area shows the three main parts of a seismic recording with its major parts, the P- and S-wave onset, the prominent Rayleigh wave and the coda, slowly vanishing in the noise.

border of human hearing capabilities. This is due to the properties of acoustic waves travelling through media. High frequency waves are attenuated with greater strength and are therefore lacking penetration capabilities needed for the deep exploration of e.g. hydrocarbons. If penetration depth is not the main focus, higher frequencies give the benefit of good spatial resolution and are therefore used for high resolution imaging techniques. The probably best known application is the ultrasound device used by doctors to construct an image of the human body and for example monitor embryos. In geophysics, due to the low penetration depth, ultrasound has only been used for small scale studies or very thorough analysis in laboratory conditions where short wavelengths are required. Nevertheless, theory developed for long wavelengths used in geophysics is transferable to ultrasonic measurements commonly used in NDT. The material properties in NDT play an important role, just like subsurface rock properties in geophysics. In concrete, strong heterogeneities and a mixture of materials (e.g. steel reinforced concrete) often cause difficulties, as they make modelling and inversion complicated due to the random interior structure with different grain sizes.

2.3 Ultrasound Propagation in Concrete as a Solid Medium

The propagation of acoustic waves through solid media is a major part of geophysics and well summarized in literature. In the following sections only the main formulas needed for the understanding of this thesis will be explained. For a detailed derivation of the description of acoustic wave propagation the reader is refered to Wapenaar (1989) or Yilmaz (2001).

2.3.1 Elastic Waves in Solid Media

In a homogeneous, isotropic and elastic solid, the equation of wave propagation is written as:

$$\rho \frac{\partial^2 \mathbf{u}}{\partial t^2} = (\lambda + 2\mu)\nabla(\nabla \cdot \mathbf{u}) - \mu \nabla \times \nabla \times \mathbf{u} \tag{2.1}$$

where ρ is the density, λ and μ are the Lamè parameters and $\mathbf{u}$ is the three dimensional displacement vector.

The velocity at which seismic body waves are propagating in an elastic medium can be derived from equation 2.1 by application of the divergence and curl operator respectively and are given by:

$$v_p = \sqrt{\frac{\lambda + 2\mu}{\rho}} = \sqrt{\frac{K + \frac{4}{3}\mu}{\rho}} \quad , \tag{2.2}$$

where K is the bulk modulus, and

$$v_s = \sqrt{\frac{\mu}{\rho}} \tag{2.3}$$

where v_p is the P-wave velocity and v_s is the S-wave velocity.

The aforementioned Lamè parameters can be expressed in terms of stress σ and Young's elastic modulus E as:

$$\lambda = \frac{\sigma E}{(1+\sigma)(1-2\sigma)} \tag{2.4}$$

$$\mu = \frac{E}{2(1+\sigma)} \tag{2.5}$$

When concrete is deformed, the stress-strain relation can only be assumed to be linear for short and small loads. Therefore, at higher load Young's modulus is no longer constant and wavespeeds are influenced by stress and strain. This effect, called the acoustoelastic effect, will later be explained and used to analyse velocity changes in a concrete beam during a loading experiment in the phases of elastic deformation.

2.3.2 Scattering and Attenuation - Frequency Regimes

In seismic exploration material changes are expected with depth, as the lithological profile of the earth changes with time. At those material boundaries, waves will be reflected, refracted and transmitted in accordance to Snell's law, depending on the acoustic impedance change between the materials and the incidence angle. When analysing concrete structures with acoustic waves on a larger scale, to detect the hidden rear wall for example, also reflections caused by acoustic impedance changes are analysed. This boundaries can for example be concrete-air or concrete-sediment boundaries.

In this work the focus is on the detection of changes of the inner structure of concrete with high frequency waves. For this analysis the scattering theory has to be used. One can see concrete as a uniform medium with a constant background velocity, which has an uncountable number of heterogeneities (Sheriff, 2002). Only a small portion of the wavefield arrives at the receiver on the direct path. These waves are called *ballistic waves*. When a wave hits one of those heterogeneities, it will change its direction, be scattered into many different directions and maybe change polarity. The amount of scattering is dependant on the wavelength and the size of the heterogeneities.

In a medium like concrete, according to Planès and Larose (2013), scattering can be separated in four main domains. First of all, the *stationary regime*, where the wavelength exceeds the macroscopic size of the structure. The *simple scattering regime*, where the wavelength is smaller than the structure size, describes the state where only weak scattering happens. As the name indicates, the *multiple scattering regime* describes multiple scattering, which happens if the wavelength is smaller than the size of the heterogeneities in the material. For concrete this heterogeneities are for example different grains of sand and gravel included in the mixture. The last regime is the *attenuation regime*, where almost no wave propagation can be observed, as the waves are strongly attenuated by scattering and absorption.

Literature values for wave-speed in concrete are about 4300 m/s for longitudinal waves and 2500 m/s for shear waves. With this velocieies e.g. Planès and Larose (2013) give the boundary frequencies between those regimes:

- Stationary regime: $f < 20$ kHz
- Simple scattering regime: $f = 20$ kHz $- 150$ kHz
- Multiple scattering regime: $f = 150$ kHz $- 1$ MHz
- Attenuation regime: $f > 1$ MHz

This can be easily verified with the relation of frequency and wavelength given by $\lambda_{p,s} = v_{p,s}/f_{p,s}$. So for example, a frequency of 60 kHz corresponds to a wavelength of 7 cm (4 cm) for P- (S-) waves. Assuming grain sizes of a maximum of 3 cm in concrete, grain related scattering, diffraction and attenuation is expected but the wavelength is still longer than the particle size and a good penetration depth is achieved. For a frequency of 150 kHz, wavelengths of 3 cm (1.5 cm) cause stronger multiple scattering, strongly limiting penetration.

There are two measures that describe the rate of scattering in a material, namely the *scattering mean free path*, l, the mean distance between two scattering events and the *transport mean free path*, l^*, the distance at which propagation is completely randomized (Fröjd, 2018). Both measures can also be seen in units of time passed until the next scatterer or the complete randomization.

It is important to note that scattering induces mode shifts. The ratio of P- and S-waves is steady for diffusive waves, as multiple scattering events lead to mode conversions. According to Snieder et al. (2002), this ratio is expressed by:

$$\frac{E_p}{E_s} = \frac{1}{2}\left(\frac{v_s}{v_p}\right)^2 \quad , \tag{2.6}$$

where E_s and E_p is the energy of the S- and P-waves and v_S, v_P are the corresponding velocities.

Using the previously mentioned velocities this ratio is around 0.098. Therefore, the signal in concrete is dominated by S-waves, even if a P-wave source is used.

With the described 'random' structure of concrete caused by the different grain-sizes, wave propagation in concrete can more or less be approximated by a random walk (Pacheco and Snieder, 2005). Figure 2.2 shows the result of a synthetic US-recording and a simulation with random-walker. Several thousand random walks through a gridded model space have been modelled with visits counted at a grid cell, acting as the receiver. At every step the intensity of the random walker (energy of the wave) is damped. One can see the similarity between the two recorded waveforms, with the direct ballistic waves at the beginning of the signal and the coda in the later part of the recording. The mentioned randomness of the scattered waves could lead to the assumption that the coda is always different in every measurement, even if the material parameters do not change. Luckily, US-propagation through concrete is perfectly reproducible under perfect conditions (Planès and Larose, 2013), as otherwise it would be impossible to gain information from the coda. A comparison of the recorded signals is actually a valuable tool to detect changes. Cracks, changing the signal, can then for example be considered as a stronger damping factor or a different decision rule for direction change (scattering) when referring to the analogy of a random walk.

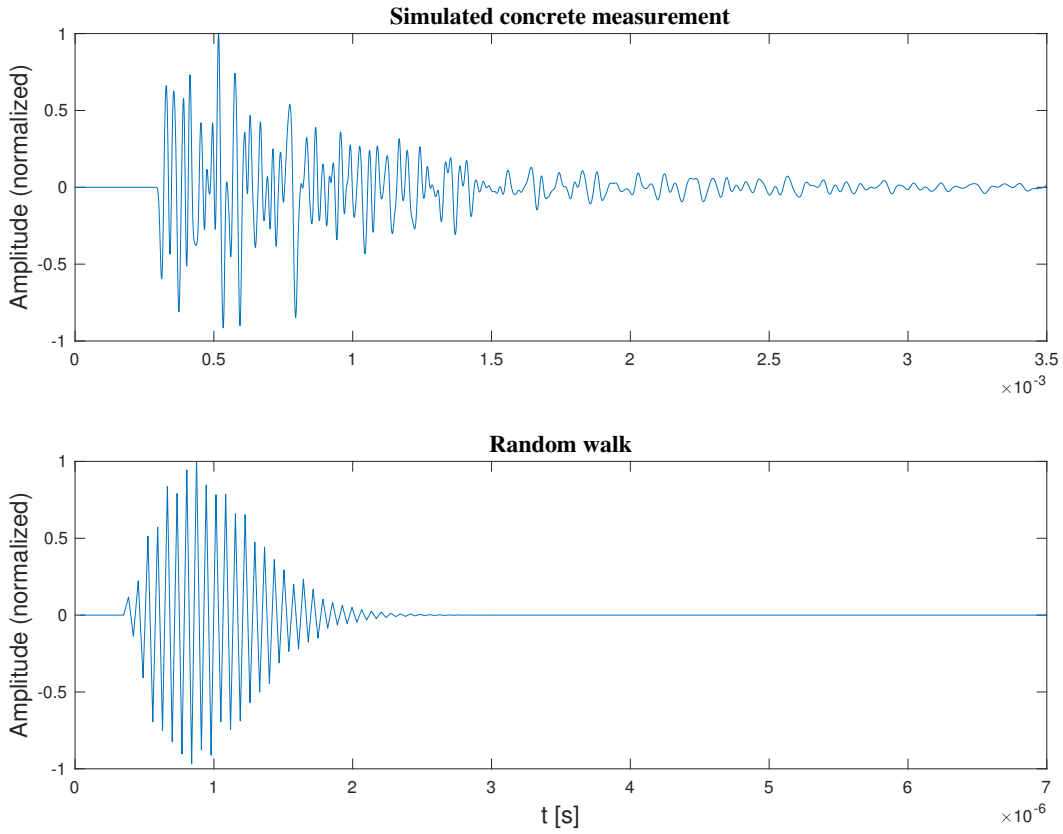

Figure 2.2: The signal shape of a recorded random walk through a grid (bottom) and a simulated measurement show similarities. In fact, the recording of ultrasound in a strongly scattering environment is often compared to a random walk in literature (see for example Pacheco and Snieder (2005))

2.3.3 Damage Indicators in Concrete

In the field of NDT the main focus is on damage detection in concrete structures. Obviously (micro-)cracks act as additional scatterers in the medium if they are big enough in relation to the wavelength. This means a crack will affect propagation of the ultrasound through the medium and, therefore, influence the recorded waveform.

Derived from this, the two basic measurement parameters which can easily be extracted from ultrasonic measurements are velocity and signal attenuation. Using classical velocity analysis for damage detection in concrete is a very difficult task, as wave velocity is not strongly affected in the early damage steps up to about 80 % of the compressive capacity of the concrete (Kamada et al., 1997). Attenuation is increased by cracking and can also be used as a possible damage detector but is influenced by coupling (Fröjd, 2018).

Both, attenuation and velocity, are in general linear properties. When concrete is put under stress, the relation of stress and strain is non-linear. The influence of this non-linear behaviour on ultrasound velocity can also be expressed in certain coefficients described by the acoustoelastic effect (see section 2.5.2).

It is important to note that there is no direct analytical connection of the parameters derived from ultrasound measurements and technical characteristics. However, the results and observations can be linked to specific behaviour of the material (Niederleithinger, 2018).

2.3.4 Diffusion Equation and Intensity Modelling

Due to the apparent random behaviour in the coda explained in the previous section, modelling and prediction of wave propagation in concrete is almost impossible. Nevertheless, there are different ways of describing a wave in a medium. As mentioned, besides velocity measurements, the intensity and attenuation of a wave are possible sources of information for the concrete's material properties and for the damage level.

The most basic model is the so called diffusive model. Diffusion, in dictionaries defined as *"the spreading of something more widely"*, describes how fast the wave spreads through the medium. This implicates that high diffusivity is expected in a medium with low scattering, while low diffusivity is expected in a scattering medium with possible damages. Therefore, one can try to detect changes in a medium with an analysis of wave diffusion. This has been shown by (Pacheco and Snieder, 2005), Deroo et al. (2010) and many more. The basic theory will be described in the following section.

The diffusion process is described by the diffusion equation:

$$\frac{\partial E(\mathbf{r},t,f)}{\partial t} - D\Delta E(\mathbf{r},t,f) + \sigma E(\mathbf{r},t,f) = S(\mathbf{r},t,f) \forall \mathbf{r} \in \Omega \tag{2.7}$$

This second order parabolic partial differential equation is describing the diffusion process with the spectral energy density $E(\mathbf{r},t,f)$[1] at distance r at time t in the solution space Ω.

[1]It is important to note that in the context of the diffusion equation E denotes energy, while in other section E is Young's modulus. Therefore, when a section in this thesis is covering diffusivity, E corresponds to energy, while in all other sections E is Young's modulus.

The diffusivity D and the dissipation rate σ are both frequency dependent. The intensity of the source is described by S. The solution of this equation of course is depending on the geometry. For the most simple case of an infinite body in d dimensions, the solution is given in Deroo et al. (2010):

$$E(\mathbf{r}, t, f) = \frac{P_0}{(4D\pi t)^{d/2}} \exp \frac{-r^2}{4Dt} \exp -\sigma t \tag{2.8}$$

with P_0 being the magnitude of the source pulse. The parameters D and σ can now be fitted with a time consuming non-linear fit, where the solution is fitted to the envelope of the seismic waveform. With a few further steps, the equation can be modified to a linear form, which is sufficient for the determination of those parameters.

Taking the logarithm of both sides of this equation one gets:

$$\begin{aligned} \ln(E(\mathbf{r}, t, f)) &= \ln(P_0) - d/2 \ln(4D\pi t) + \frac{-r^2}{4Dt} - \sigma t \\ \underbrace{\ln(E(r, t, f)) + d/2 \ln(t)}_{f(A,B,C,t)} &= \underbrace{\ln(\frac{P_0}{(4D\pi)^{d/2}})}_{A} + \underbrace{\frac{-r^2}{4Dt}}_{B/t} + \underbrace{-\sigma t}_{Ct} \end{aligned} \tag{2.9}$$

with the resulting linear equation:

$$f(A, B, C, t) = A + B/t + C * t \tag{2.10}$$

the parameters A,B and C (and the parameters D and σ respectively) can now be determined by solving this linear system of equations (compare to Deroo (2009)).

There are solutions to the diffusion equation (2.7) for different geometries, which are for example shown in Planès and Larose (2013). However, equation 2.8 will be sufficient for the purpose of this thesis, as it is a fast and convenient way of parameter extraction with possible use in monitoring.

With an estimated value for diffusivity D, Sheng (1995) (as cited in Fröjd (2018)) shows that the transport mean free path, previously described as the distance at which propagation is completely randomized, can be calculated with a simple relation including the dimensionality d and the velocity v_e of the waveform's envelope:

$$l^* = \frac{dD}{v_e} \tag{2.11}$$

The transport mean free path can be used as an indicator for the length and position of the CWI window, which will be explained in 2.4. As the diffusion model is not accurate for waves that have travelled less than one transport mean free path (Fröjd, 2018), it has been proposed to use the radiative transfer intensity model. This will not be explained in further detail, but the reader is refereed to Chandrasekhar (1960) or Ishimaru (1978) for additional information.

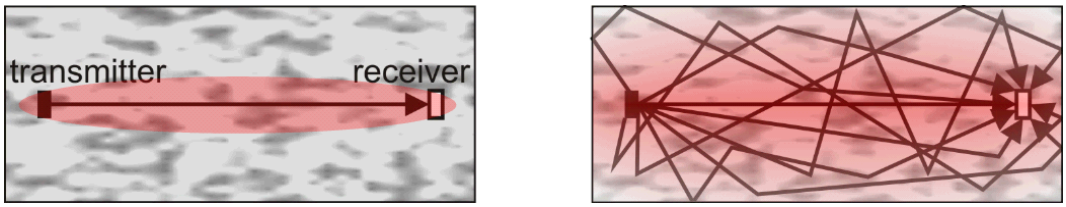

Figure 2.3: The ballistic wave travels directly from source to receiver (right), while the scattered coda waves cover a larger area of concrete before beeing recorded (right). Image from Niederleithinger et al. (2018)

2.3.5 Sensitivity

Knowing the diffusive behaviour of ultrasound, it is possible to gain information on the area a specific measurement is sensitive to. Using the speed of energy spreading and the scattering mean free path, it is possible to calculate sensitivity kernels. The construction of sensitivity kernels has been shown e.g. in Pacheco and Snieder (2005) and is relying on the probable wave paths from source to receiver. If it is likely, that a wave passes a certain area, the measurement is sensitive and capable of detecting changes in this very area. If there is only little or no chance of a wave making its way from source to receiver while passing the area of interest, the measurement is not sensitive to this area. In general, the area of high sensitivity is approximately of the same scale as the transport mean free path in the area around the source and receiver (Fröjd, 2018). With bigger distances, the sensitivity decreases. This shows that, even if scattering means loss of directional information, there is still some location information left in a measurement. This principle is used in the LOCADIFF algorithm developed by Planès, Larose and Rosseto used for inversion of CWI results for damage detection (see for example Larose et al. (2010) or Rossetto et al. (2011)).

2.4 Coda Wave Interferometry

In most applications with seismic and therefore also ultrasonic data, the arrival times of P- and S-waves are used for analysis. When travel-time differences become very small, for example due to short distances or only minor material changes, those techniques reach their limitations.

The coda, which is as mentioned before the later part of a seismic waveform, is composed of multiply scattered waves in the medium. This means that the waveforms recorded at later times in the coda have spent longer time in the medium and cover not only the direct wave-paths of the ballistic waves. As figure 2.3 indicates, the recorded signal at the receiver location is a summation of waves that have travelled along multiple trajectories T. Mathematically formulated, the recorded signal - in the case of an unperturbed wavefield $u_u(t)$ - would then simply be (as described in Niederleithinger et al. (2018)):

$$u_u(t) = \sum A_T(t) \tag{2.12}$$

where $A_T(t)$ is the amplitude of the wave that has travelled along each trajectory T.

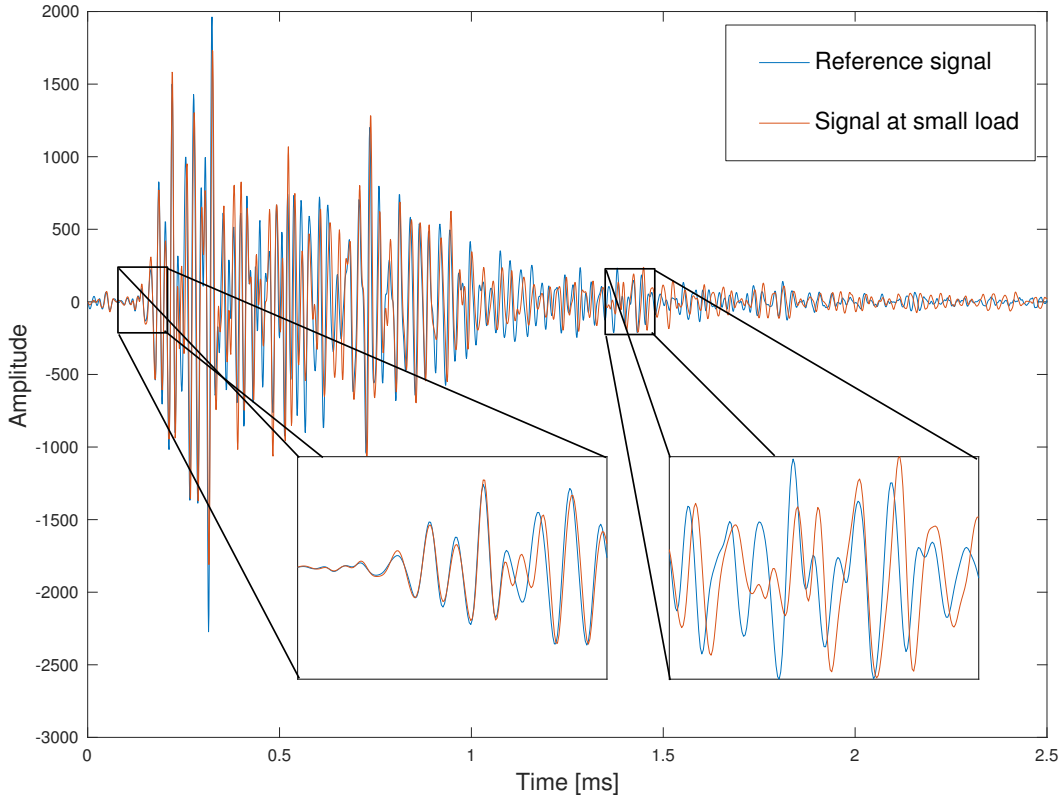

Figure 2.4: The difference between the reference signal and a measurement under load is minimal in the first arrivals. In a later part of the signal the differences become clearly visible.

As mentioned beforehand, a perturbation of the medium results in a travel-time shift (τ_T) in the recorded signal:

$$u_{pt}(t) = \sum A_T(t - \tau_T) \tag{2.13}$$

The time shift will be visible in the recorded waveform. Maybe as an apparently slower propagation velocity analysed with TOF analysis, but almost certainly in the coda part of the recording. This behaviour is shown in figure 2.4, where one can clearly see a difference in the coda which is only minimal in the first arrival.

As mentioned in previous sections, the coda is more sensitive to cracks in the area as it is spending more time in the medium (see figure 2.3). To analyse the degree of perturbation between two recordings an analysis of the correlation of both is necessary. There are several methods for the calculation of an correlation coefficient (CC) between two recordings. For CWI, the cross correlation is used, which can be done both in time and frequency domain (Planès and Larose, 2013). The cross correlation coefficient between two waveforms (on a time window between t_1 and t_2) is calculated by:

$$CC(t) = \frac{\int_{t_1}^{t_2} u_u(t) u_{pt}(t) dt}{\sqrt{\int_{t_1}^{t_2} u_u^2(t) dt \int_{t_1}^{t_2} u_u^2(t) dt}} \tag{2.14}$$

where again u_u is the unperturbed waveform and u_{pt} is the perturbed waveform. The CC value will be between 0 and 1, where 1 indicates exact agreement between the two recorded waveforms.

The cross-correlation coefficient is a measure of similarity of two wave recordings in a certain time window. A comparison of measurements acquired over time gives information whether or not any changes have occurred in an area between the sensors. When the coefficient is decreasing over time, damage can be expected and further evaluation will be necessary. The time windows used for the CC calculation should be evaluated thoroughly, as there need to be several periods included in the signal. Mainly the coda is to be used and late arrivals below a certain signal to noise ratio (SNR) should be excluded to reduce the influence of random ambient noise sources (Planès and Larose, 2013).

Of course, one wants to link the differences in the recorded waveform to a physical quantity. The two main techniques enabling a determination of a change of velocity dV/V_0 will be described now according to the summary paper for CWI published by Planès and Larose (2013).

2.4.1 Doublet Technique

One of the first methods to calculate a velocity change is the so called doublet technique. Two short signal parts are compared with the cross correlation. The change in velocity is assumed to be manifested in a time shift of the signal. As the compared signals are in relatively short time windows, this time shift can be assumed to be constant. The CC is calculated several times for different time shifts (δt) of the perturbed signal:

$$CC(t, \delta t) = \frac{\int_{t-T}^{t+T} u_u(t) u_{pt}(t + \delta t) dt}{\sqrt{\int_{t-T}^{t+T} u_u^2(t) dt \int_{t-T}^{t+T} u_u^2(t) dt}} \tag{2.15}$$

The time shift maximizing the CC is used for calculation of the velocity change, as it is assumed to be linearly dependent:

$$\frac{\delta t}{t} = -\frac{\delta V}{V_0} \tag{2.16}$$

This calculation is repeated several times for several time windows in the coda to obtain a robust result for a velocity change between two ultrasonic measurements. The fact that many cross-correlations have to be calculated for many time windows makes this process computationally expensive and time consuming.

2.4.2 Stretching Technique

As the velocity change is certainly not a simple delay in time over a longer time window, a more sophisticated method, called stretching method, has been introduced ((Lobkis and Weaver, 2003) or (Sens-Schönfelder and Wegler, 2006)). Again the recorded signal in a time window is compared to a reference signal. The stretching method is not a simple comparison

of the recordings with different time shift, but the reference coda is stretched by interpolation at times $t(1+\alpha)$ (Fröjd, 2018). α is the so called stretching factor and the factor α_i maximizing the correlation coefficient is considered to be the coefficient relative to the velocity change in the material:

$$CC(t,\alpha) = \frac{\int_{t_1}^{t_2} u_u(t+\alpha)u_{pt}(t)dt}{\sqrt{\int_{t_1}^{t_2} u_u^2(t+\alpha)dt \int_{t_1}^{t_2} u_u^2(t)dt}} \tag{2.17}$$

A major advantage of the stretching method is that the window can be chosen to be much larger and include several periods, while the doublet technique requires several small windows to be averaged in the end. This makes the technique more stable in noisy environments, as small local disturbances in the signal are compensated by the window length (Planès and Larose, 2013). Nevertheless, the starting point and length of the time window has to be evaluated according to the measurement parameters. It is proposed (e.g. in Zhang et al. (2016)) to use the transport mean free time, the time which a ultrasound signal has travelled until it looses its directional information due to scattering, as a selection criterion for the CWI window. The window should start at a point way beyond the transport mean free time and be long enough to include several transport mean free times. This process could be automated with a calculation using e.g. the diffusion equation (chapter 2.3.4). However, very often a visual analysis of the recorded signal gives enough information to select a time window containing enough coda without falling below the SNR in the later parts of the signal.

2.4.3 Stepwise CWI Method

If the structural properties change, classical CWI, where the measurement is compared to a fixed reference, will produce low CC values, as the signal forms will probably change significantly due to environmental influences or cracks. As monitoring tasks are long term projects, this might cause some problems, as possible damage might be overshadowed by long time material changes which are expected in concrete structures. Therefore, it has been proposed by Niederleithinger et al. (2018) to change the practice from having a fixed reference signal to a variable choice of reference signal. This procedure is called stepwise CWI.

In general, there are two different approaches to stepwise CWI. The first and most basic is to just set the reference signal to the previous measurement when calculating the velocity change. In this way a high similarity of both signals is guaranteed if no severe damages have occurred in the reasonably short timespan between both measurements. This method is computationally very expensive, as the reference signal has to be stretched and interpolated every time, while this step has to be taken only once for the fixed reference method. Therefore, in an alternative approach, the reference signal is only changed if the difference between recorded and reference signal are too big, meaning if the CC coefficient is falling below a certain threshold.

As this method also produces velocity changes between two measurements, it is possible to calculate a cumulative velocity change to reference the velocity differences to the beginning of the experiment. The calculation of the cumulative velocity change is subject to rounding errors, which increase the discrepancies between calculated velocity change and real velocity changes over time. A cumulative calculation of the CC coefficient is not possible, as this technique is non-unique (Niederleithinger et al., 2018).

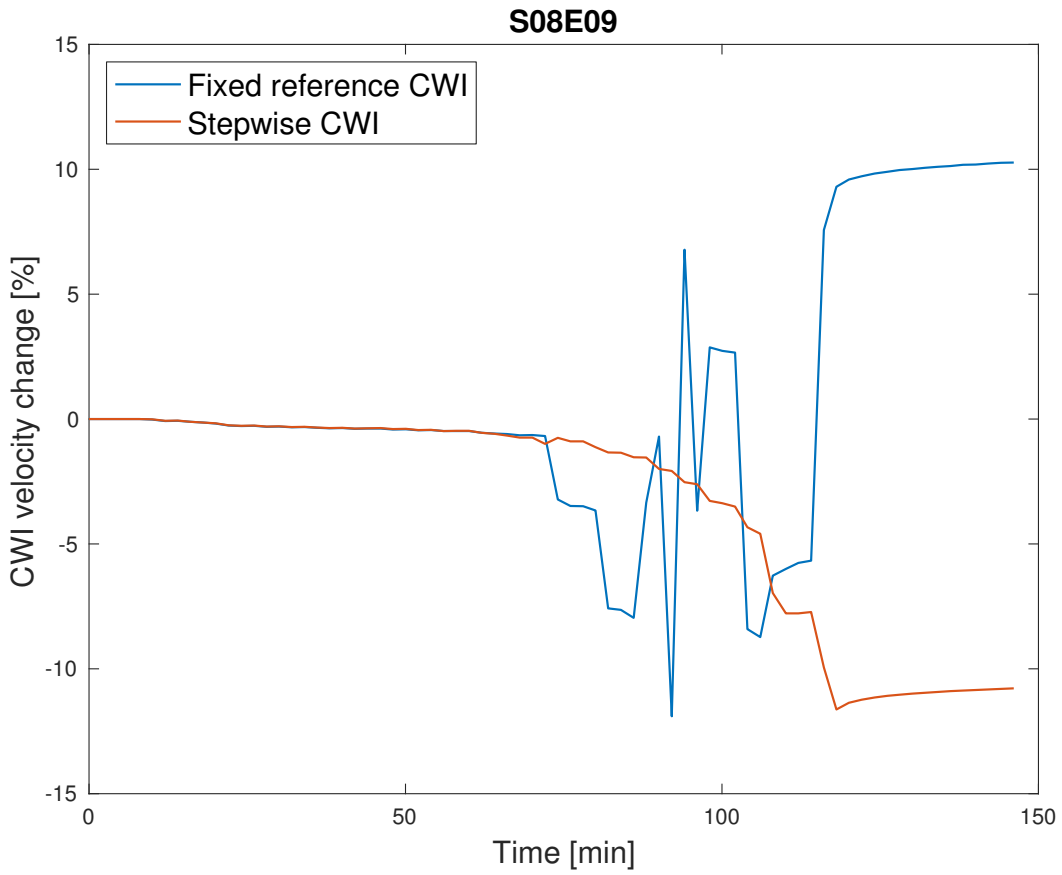

Figure 2.5: The stepwise CWI velocity change during a loading experiment clearly proves to be stable for a longer time. At some point, the material changes are too big and a comparison of the first measurement before loading and the measurement in a later time-step are too different for the fixed reference CWI stretching method to produce stable results.

Niederleithinger et al. (2018) have shown that their method of coda analysis produces stable results for a longer time than the classical fixed reference CWI. This is shown in figure 2.5.[2]. When load is increasing and damages occur, both CWI methods indicate bigger velocity change but the stepwise CWI remains stable for a longer time. In the first phases of loading, both results are (almost) identical. Therefore, this method is an important tool for long time monitoring, as a change of reference signal will be necessary after time to produce reliable results, while it was shown that the reference to the initial velocity can be maintained.

2.4.4 Method in this Thesis

In this thesis, mainly the fixed reference CWI will be used, as focus will be on the early stages of deformation, where both methods produce good results and the fixed reference CWI

[2]In this thesis I have chosen to plot the CWI velocity change with its original sign in order to improve the display of results in later sections. The reader should be aware of the practice of plotting the negative CWI velocity change (as in Niederleithinger et al. (2018)) Both ways are possible and the choice is mostly linked to displaying reasons.

is simply faster and not susceptible to rounding errors for the calculation of the velocity change. Nevertheless, when extending the analysis to the later phases of deformations, it will be necessary to use the stepwise procedure.

2.5 Concrete Under Load

The monitoring of bridges over time is a task of investigating the change of concrete during and after various phases of loading. For bridges, this will mainly be cars and trucks passing by but also other exterior forces might act on the concrete structure and affect its inner integrity by inducing cracks. The reaction of concrete to loading tests is a well studied field of civil engineering. The way concrete responds to loading, is separated into several deformation steps. As many other materials, concrete can be elastically or plastically deformed, as well as loaded until brittle failure. All of this has an influence on the acoustic wave propagation through concrete and these relations will be summarized in the following sections.

2.5.1 Linear Elasticity - Hooke's Law

The theory about linear elasticity and Hooke's law presented here is only a brief summary of Gould and Feng (1994, Chapter 4) to illustrate the relations used for later analysis. For an extensive derivation of the given relations, the cited book is recommended.

In the early stages of loading, before any plastic deformation or even concrete failure is expected, the deformation of concrete can be approximated by Hooke's law. Hooke's law describes a relationship between stress and strain in a medium. For anisotropic, continuous three dimensional media Hooke's law is given by:

$$\sigma_{ij} = C_{ijkl}\epsilon_{kl} \quad \text{for} \quad i,j,k,l = 1,2,3 \tag{2.18}$$

Where σ_{ij} is the stress tensor and ϵ_{kl} is the strain tensor. C_{ijkl} is the fourth order stiffness tensor, which has $3*3*3*3 = 81$ elements. One can use several symmetry relations to reduce the number of components in the stiffness tensor.

For isotropic materials the stress-strain relation in three dimensions (using the lame constants λ and μ) is given by:

$$\sigma_{ij} = 2\mu\epsilon_{ij} + \lambda\delta_{ij}\epsilon_{kl} \quad , \tag{2.19}$$

where δ_{ij} is the Kronecker delta.

Under plane stress, which is often the case in idealised load experiments on concrete, $\sigma_{12} = \sigma_{21} = \sigma_{13} = \sigma_{31} = \sigma_{23} = \sigma_{32} = \sigma_{33} = 0$ and equation 2.19 reduces to two principal stress/strain components.

Two important quantities often used in connection with the stress strain relation are Poisson's ratio

$$\nu = \frac{\lambda}{2(\mu + \lambda)} \tag{2.20}$$

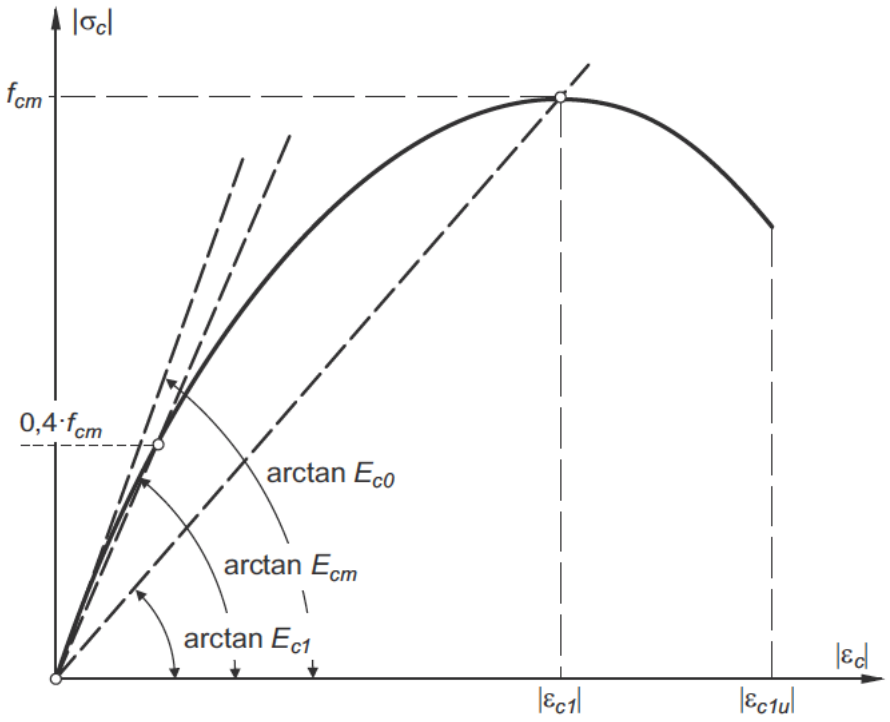

Figure 2.6: The stress-strain curve for concrete (according to DIN 1045-1) only shows approximate linear behaviour for small stresses. The different E-moduli indicated in the picture were introduced for different purposes but for the standard linear elastic deformation E_{cm} is used. Image from Zilch and Zehetmaier (2006).

and Young's modulus

$$E = \frac{\mu(2\mu + 3\lambda)}{\mu + \lambda} \quad . \tag{2.21}$$

As figure 2.6 shows, the linear elastic behaviour described by Hooke's law is only valid for the small loads up to approximately $|\sigma_c| \approx 0.4 f_{cm}$, where f_{cm} is the compressive strength of the concrete. Afterwards, the relationship becomes non-linear but deformation is still assumed to be elastic. The linear relation in the early stage is also only valid for short term loading but not for permanent load models (Zilch and Zehetmaier, 2006). In stages of higher compression ($> f_{cm}$), the relationship is no longer elastic.

2.5.2 Non-linear Elasticity - Acoustoelastic Effect

Looking back to section 2.3.1, one can see the link of wave velocity and Young's modulus (E) derived from the stress-strain relation. If this relation is not linear, Young's modulus can no longer be assumed to be constant when the stress-strain relation becomes non-linear. Therefore, it is necessary to describe the non-linear behaviour of stress-strain linked to the velocity of waves in a medium like concrete. This relationship is described in the acoustoelastic

theory. The mathematical description of this non-linearity is done by the consideration of second order effects, which is expressed by the introduction of a 6th order tensor to Hooke's law (compare to equation 2.18; (Stähler et al., 2011)):

$$\sigma_{ab} = c_{abcd}\epsilon_{cd} + C_{abcdef}\epsilon_{cd}\epsilon_{ef} \tag{2.22}$$

As for the linear case in the previous chapter, the number of parameters reduces if the medium is isotropic. The 6th order tensor is then expressed by the Munaghan constants k, l, m. This parameters can be seen as the second oder parameters, while the Lamè parameters λ and μ are the first order parameters. The derivation of this relations has first been published in Murnaghan (1937).

According to Toupin and Bernstein (1961) (as cited in Stähler et al. (2011)), the wave speeds in compressed media depend on direction and polarization and can be expressed depending on the Murnaghan parameters. It has been shown in Payan et al. (2010) that this theory can also be applied to concrete in laboratory experiments to derive the Murnaghan parameters.

Both, a comparison of equations 2.18 - 2.22 and figure 2.6 indicate the non-linear strain dependency of Young's modulus E. This nonlinearity can be separated in a classical and non-classical part, where the non classical part is related to material hysteresis (Payan et al., 2010). The nonlinearity of E in a 1-D case can be described by (according to Chen et al. (2010) as cited in Jin et al. (2017)):

$$E = E_0[1 + \beta\epsilon + \delta\epsilon^2 + \underbrace{\cdots + \alpha(\Delta\epsilon + sign(\dot{\epsilon})\epsilon)}_{\mathcal{O}(\Delta\epsilon,\dot{\epsilon},\alpha)}] \quad , \tag{2.23}$$

where E_0 is the classical linear elastic modulus, β the quadratic, δ the cubic, classical non-linear parameters (which are depending on the a combination of Murnaghan's parameters) and α the non-classical, non-linear parameter. $\Delta\epsilon$ is the maximum strain amplitude and $\dot{\epsilon}$ the strain rate. *sign* corresponds to the sign-function. Its value depends on the sign of $\dot{\epsilon}$. The focus of this thesis will be on the evaluation of the classical non-linear parameters. Therefore the non-classical part is summarized in $\mathcal{O}(\Delta\epsilon, \dot{\epsilon}, \alpha)$.

According to Jin et al. (2017), the ratio of change in Young's modulus can be approximated by the rate of change in velocity of high frequency waves. Therefore, CWI results can be used for evaluation of the classical non-linear parameters in concrete:

$$\frac{\Delta V}{V_0} = \frac{1}{2}\frac{\Delta E}{E_0} = \frac{1}{2}(\beta\epsilon + \delta\epsilon^2) + \mathcal{O}(\Delta\epsilon, \dot{\epsilon}, \alpha) \tag{2.24}$$

Chapter 3

Experiment

In a joint project of the German Federal Institute for Materials Research and Testing (Bundesanstalt für Materialforschung und -prüfung (BAM)) and Aachen University (Rheinisch-Westfälische Technische Hochschule (RWTH)) on behalf of the federal highway research institute (Bundesanstalt für Straßenwesen (BASt)), several reinforced concrete beams simulating bridge girders were built. Those girders were equipped with different measurement devices, including embedded ultrasonic transducers and concrete and steel strain gauges. The five girders built at RWTH Aachen were loaded stepwise up to failure and measurements were taken during the entire loading process. All recorded data is provided for BAM for research purposes. Parts of the research on the ultrasoinc data from this experiment has already been published in Niederleithinger et al. (2018).

3.1 Objective of the Experiment

The goal of the experiment was to measure changes in concrete during loading, crack development and failure on a large structure of dimensions similar to bridge constructions. The main objective of BAM is the detection of (micro-)crack development with the embedded ultrasonic sensors, to better understand the ultrasound data and compare the results of a large scale experiment - where the concrete sample is not perfectly designed for the experiment but the experiment is limited by practical construction requirements and practices - to other studies.

The other measurements (e.g. the strain gauges) were conducted by RWTH in order to measure the material behaviour mainly in the non-linear and elasto-plastic phase of deformation, as well as shortly before failure, for different geometries and reinforcements.

3.2 Bridge Girders

For this experiment, five bridge girders were used in loading experiments. They will in the following sections be regarded to as DLT 1.1-1.5.

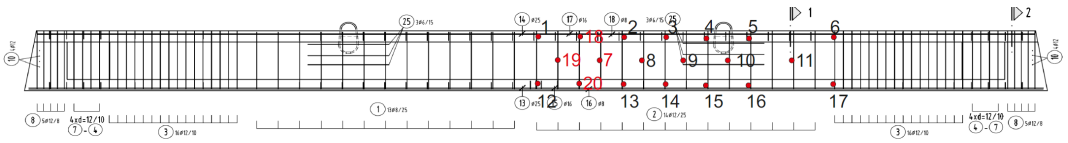

Figure 3.1: Profile of the girder 1.3 with indicated locations of the US sensors. (Image from Niederleithinger (2018))

Table 3.1: Excerpt of concrete parameters

Girder number	Geometry	Stability class	Compressive strength $[N/mm^2]$	Young's modulus $[N/mm^2]$	Prestress $[MPa]$
DLT 1.1	Rectangular	C30/37	51.21	25 842	2.5
DLT 1.2	I-profile	C30/37	41.97	27 237	2.5
DLT 1.3	I-profile	C30/37	40.58	25 833	2.5
DLT 1.4	Rectangular	C30/37	47.57	23 369	2.5
DLT 1.5	I-profile	C30/37	47.32	26 618	2.5

3.2.1 Geometry and Concrete Parameters

For the experiment, two different girder geometries have been used. DLT 1.1 and DLT 1.4 had a rectangular profile, DLT 1.2, 1.3 and 1.5 an I-profile. All girders had a length of 12.0 m and were 0.80 m high. The web width was 0.25 m for all girders. The I-profiles had a top width of 0.75 m and a bottom width of 0.55 m with a flange height of 0.15 m. The girders were prestressed with 2.5 mega pascal (MPa). Figure 3.1 shows the schematics of girder DLT 1.3. All five girders are separated into two halves with different reinforcement strength. The ultrasonic measurements - the position of the transducers is also indicated in figure 3.1 - are only conducted in the half of the girder with stronger reinforcement, so the focus of the analysis in this thesis will be on this half only. For all five girders the same type of concrete (C30/37 according to DIN EN 206-1/DIN 1045-2) was used. The main concrete parameters can be found in table 3.1.

3.2.2 Loading Phase

For the loading experiment, girders 1.1-1.3 were loaded until failure in single load experiments. Two loads were pressing on both halves of the girder, which was resting on three bearing points. DLT 1.4 and 1.5 were homogeneously loaded over the whole girder. In both cases the load was increased stepwise, with periods of constant load in between. The two different loading setups are shown in figure 3.2 for the single load experiments and in figure 3.3 for the homogeneous load experiments. In reality, DLT 1.4 and 1.5 were horizontally rotated by 180° for practical reasons.

The load applied to girders DLT 1.1-1.3 was stepwise increased by 50 kN. In the homogeneous load tests the increment of press force was 10 kN per single loading barrel. Before failure of the half with weaker reinforcement, the loading experiment was stopped and the girder stabilized by application of additional shear stresses counteracting the load induced shear tensions. This

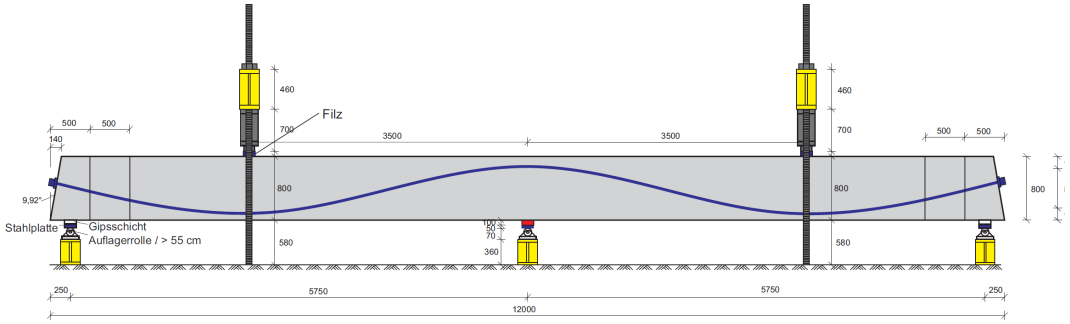

Figure 3.2: Experiment setup for girders 1.1, 1.2 and 1.3 with two single loads applied to the girder. The girder is resting on three bearing points. (Image created by RWTH Aachen)

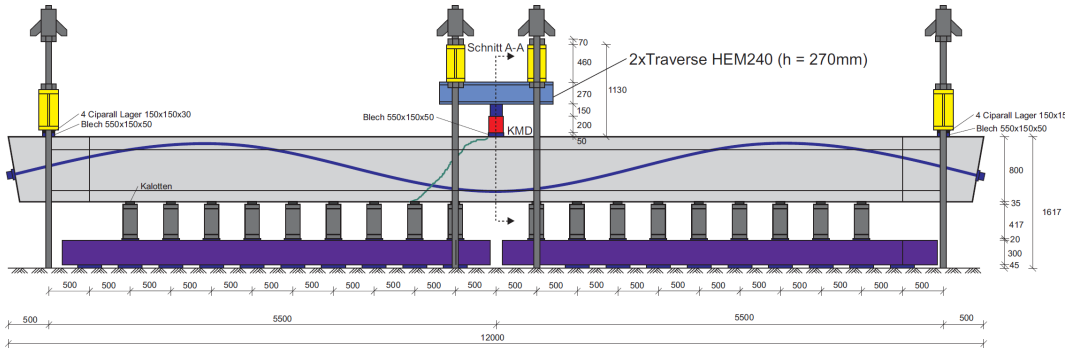

Figure 3.3: Setup of the experiment for girder 1.4 and 1.5 with a stepwise homogeneous load on the whole girder. In reality the experiment was built upside down for practical reasons. (Image created by RWTH Aachen)

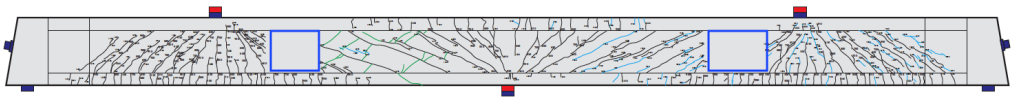

(a) DLT 1.3

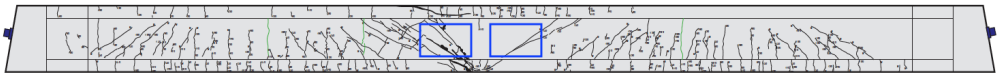

(b) DLT 1.5

Figure 3.4: Cracking pattern after loading experiment for DLT 1.3 (a) and DLT 1.5 (b). The rectangular sections do not show any recorded cracks, as digital image correlation was done in this area. Nevertheless, the cracking pattern continues throughout this areas. (Images modified from the original created by RWTH Aachen)

procedure failed for DLT 1.4. Therefore, this experiment had to be stopped earlier. In the second half of the experiment the girders were loaded until failure.

For DLT 1.3 first cracks in the main shear zones below the loading points appeared at a load of 500 kN. From that point onwards, cracking continued originating from the loading points in a triangular pattern. Figure 3.4 (a) shows the pattern on DLT 1.3 at the end of the loading experiment but before failure. For DLT 1.1 and 1.2 the patterns develop in a similar way throughout the experiment.

For DLT 1.5 the pattern is shown in figure 3.4 (b). As a homogeneous load is applied in those experiments the pattern differs compared to DLT 1.1 - 1.3. Small cracks already develop at 30 kN load (per loading barrel) and severe cracking starts between 60 kN and 90 kN. Cracking again starts in the areas of highest tensile stress on the opposite side of the loading barrels and is strongest in the center between two cushions.

3.3 Measurement

3.3.1 Embedded Ultrasonic Sensors

BAM embedded ultrasound piezoelectric P-wave transducers of type ACS S0807 into all five girders. The transducers were developed by ACS as a special order from BAM. Their characteristics have been analysed by BAM, as published in Niederleithinger et al. (2015). The embedded transducers are designed for longevity (Niederleithinger, 2018), as monitoring should be performed over a long timespan and maintenance of such embedded sensors is impossible without destruction of the bridge. Figure 3.5 shows an image of the sensor with its dimensions and the way it is attached to the reinforcement bars in this experiment before concreting. The setup for every girder was slightly different to also compare different sensor geometries. Table 3.2 gives an overview over the transducer setup in the girder.

Figure 3.6 and figure 3.7 show a detailed map of the US-transducers with the used combinations for girders 1.3-1.5, as shown in Niederleithinger (2018). The focus of data analysis

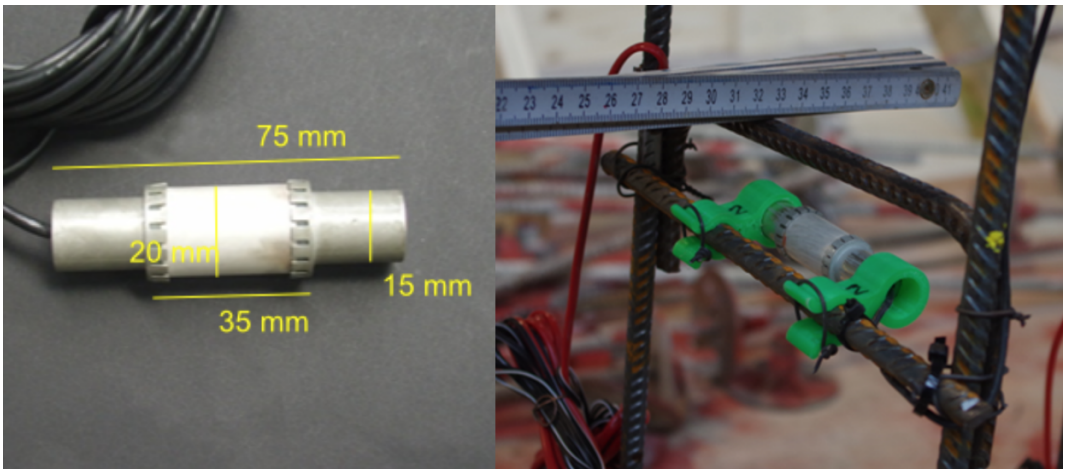

Figure 3.5: ACS S0807 transducer with its dimensions (left) and attached to the reinforcement bars before concreting (right). (Photos from Niederleithinger (2018))

Table 3.2: US Geometry parameters for the different girders

	DLT 1.1	DLT 1.2	DLT 1.3	DLT 1.4	DLT 1.5
Number of transducers	8	8	20	10	10
Number of transmitter-receiver combinations	14	16	48	27	27
Distances	0.3 - 1.75 m	0.3 - 1.75 m	0.3 - 1 m	0.5 - 1 m	0.5 - 1 m
Geometry	Irregular	Irregular	Grid	Grid	Grid

will be on girders 1.3 and 1.5, as they have shown to provide the best data with a grid-like geometry and more source-receiver combinations.

During the whole loading experiment, the measurements were repeated for all used transmitter-receiver combinations every two minutes. The transmitter emitted a box shaped pulse with a central frequency of 60 kHz. 5 ms were recorded for every pair and measurement. All parameters are summarized in table 3.3.

Table 3.3: US measurement parameters

Parameter	Value
Central frequency f_0	60 kHz
Signal shape	rectangle
Recording time	5 ms
Sampling frequency f_s	1 MHz
Averaging	1-12
Measurement interval (during loading)	2 min

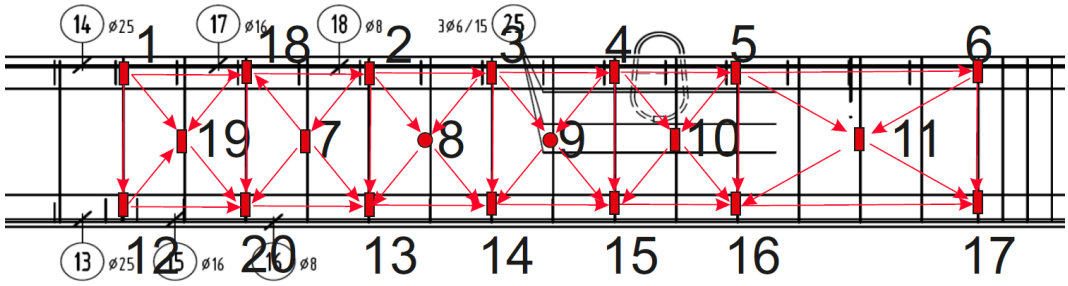

Figure 3.6: Geometry and source-receiver combinations for DLT 1.3. The blue line indicates the tension duct. (Image from Niederleithinger (2018))

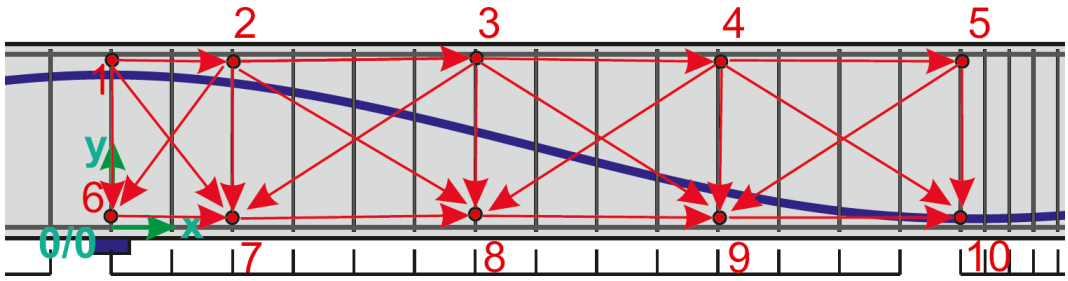

Figure 3.7: Geometry and source-receiver combinations for DLT 1.4 and 1.5. The blue line indicates the tension duct. (Image from Niederleithinger (2018))

3.3.2 Other Sensors

In addition to the ultrasonic transducers from BAM, RWTH Aachen attached and embedded their own sensors to the girders:

- concrete strain gauges (embedded)
- steel strain gauges (embedded)
- inductive displacement sensors
- load cells

Furthermore, a *Digital Image Correlation* (DCI) was used on parts of the girders for crack detection.

Figures 3.8 and 3.9 show the geometry of the aforementioned sensors with the following nomenclature. KMD are the load cells, D#D are the concrete strain gauges and all other sensors are inductive displacement sensors. The steel strain gauges are not shown but attached to all vertical reinforcement bars except in the densely reinforced areas on the right and left side of each girder (see figure 3.1).

One can see that the inductive displacement sensors were on the one hand used as deformation gauge rosettes and on the other hand to measure bending vertically and horizontally (indicated by Bi and Du in the schematics).

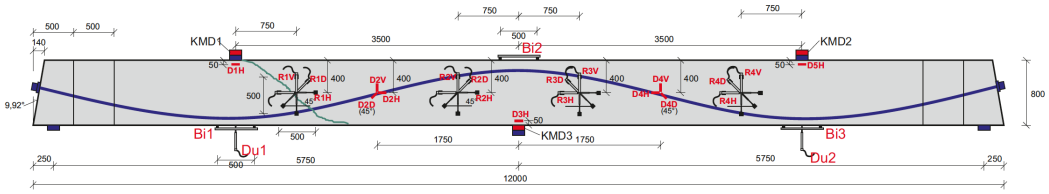

Figure 3.8: Schematics of the sensor applications to girders 1.1-1.3. (Image created by Dr. Martin Herbrand)

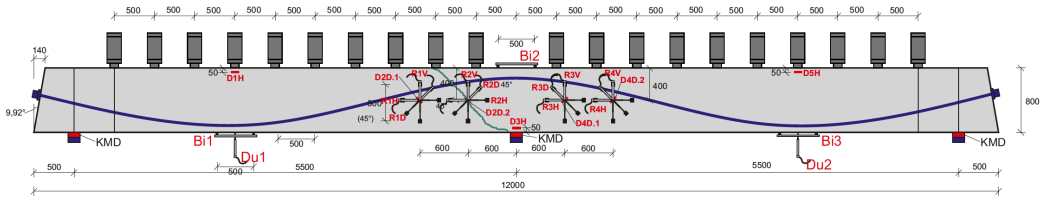

Figure 3.9: Schematics of the sensor applications to girders 1.4/1.5. (Image created by Dr. Martin Herbrand)

The sensors can therefore measure the load applied to the structure, the (punctual) strains in the concrete and reinforcement, as well as the level of deflection caused by the loading. The last mentioned measurement is always in the middle of two bearing points, as the biggest deflection is expected there. Compared to the ultrasonic measurements with a repetition rate of two minutes, this sensors recorded almost continuously during the whole loading experiment.

3.4 Data Preprocessing

3.4.1 US Measurements

For the ultrasonic measurements several preprocessing steps have to be taken. Figure 3.10 shows the raw recorded waveform of the source receiver combination S08E09 (where S is the source and E is the receiver with the corresponding number) in girder DLT 1.3 compared with the signal used for CWI later on.

In this experiment, the recording started shortly before the trigger of the US-transmitter to determine the noise level (Niederleithinger et al., 2018). This pretrigger part has to be removed first. Furthermore, the vertical offset in amplitude introduced by drifts of the sensor has to be compensated, so the pre-onset amplitude level is around zero. The first peak seen in the raw recoring is the cable crosstalk at the time of triggering which needs to be removed as it is no singal from wave propagation through the concrete. The last and final step is the classical frequency filtering known from standard seismic processing to suppress unwanted high and low frequency noise and long wavelength trends in the signal. With a central frequency of 60 kHz excited from the transducer, a bandpass filter of 1-5-150-300 kHz was chosen to avoid

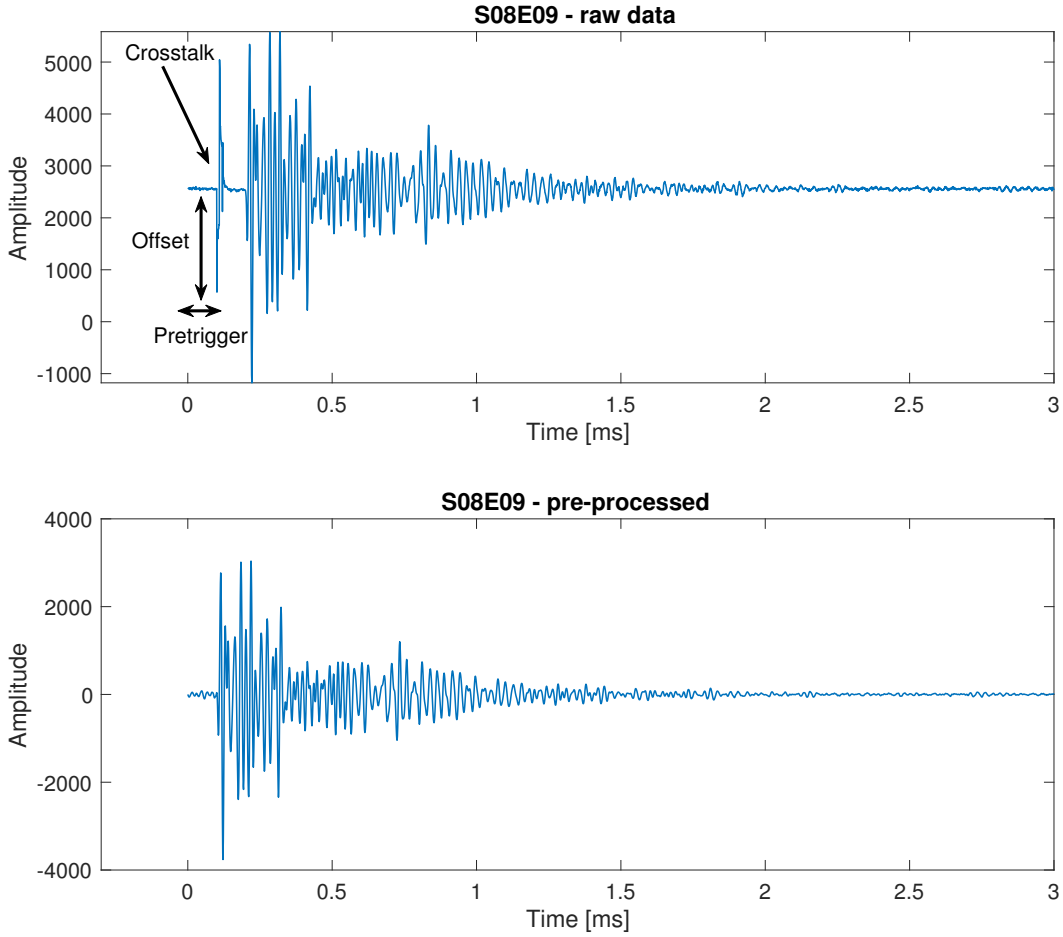

Figure 3.10: Pre-processing steps required for an analysis of the US data with CWI (top) and the resulting signal.

exclusion of signal response but exclude unwanted noise. The filter parameters are follwoing the choices made for previous publications on this dataset by Niederleithinger et al. (2018) and Niederleithinger (2018).

3.4.2 Strain Measurements

The measurements by RWTH were transformed to SI units when necessary. The measured "way change" from the inductive displacement sensors has to be normalized by the length of the sensors to get a strain value averaged over the area, while the embedded concrete strain gauges already deliver a punctual value at the point of implementation into the structure. The main (pre-)processing task required for the following analysis is the calculation of the main-strain (and its direction), which can be done for rectangular rosettes like the ones used here with the following formulas (adapted from Dankert and Dankert (2013)):

$$\epsilon_{1,2} = \frac{\epsilon_H + \epsilon_V}{2} \pm \frac{1}{\sqrt{2}} \sqrt{(\epsilon_H - \epsilon_D)^2 + (\epsilon_D - \epsilon_V)^2} \tag{3.1}$$

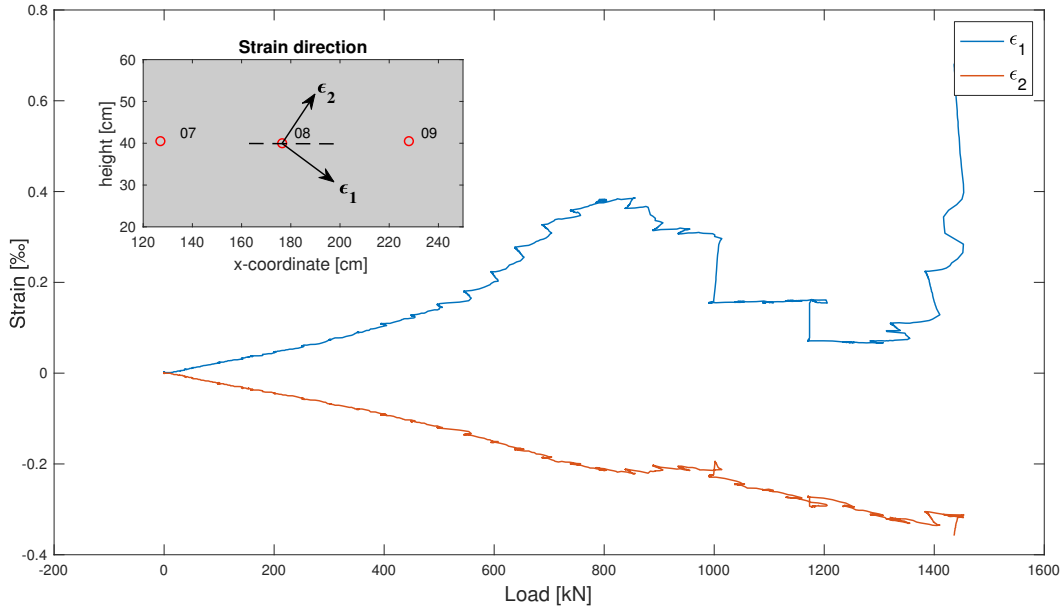

Figure 3.11: The strains ϵ_1 and ϵ_2 in the two main directions can be calculated from the measurement of the embedded concrete strain gauges. Here D4 (see figure 3.8) is taken in DLT 1.3. The strain is plotted over the load in kN. The red circles in the section of the girder displayed on the top left indicate US-sensor positions. One can see the extension in direction of ϵ_1 and the compression in direction of ϵ_2. The pre-stressing of the girder is counteracting the extension.

for the value of the extension (ϵ_1 using plus) and compression (ϵ_2 using minus) main strain, where ϵ_H is the horizontally measured strain, ϵ_V the vertically measured strain and ϵ_D the strain measured diagonally in a 45° angle to the horizontal axis and

$$\Theta = \frac{1}{2}\tan^{-1}\left(\frac{\epsilon_H - 2\epsilon_D + \epsilon_V}{\epsilon_H - \epsilon_V}\right) \tag{3.2}$$

for the angle of the direction of the main strain. The angle is expressed as the angle between the main strain direction and the used calculation grid, which is the angle towards the horizontal axis for the used sensors.

Figure 3.11 shows the strain in the two main directions at the indicated position in girder DLT 1.3. Positive strains indicate extension, negative strains indicate compression. The direction of extension perfectly fits the direction of the cracks (see figure 3.4). At high loads the measurement gets unreliable, as stress and strain are released by cracking.

Chapter 4

Results

4.1 Diffusivity Analysis

Before CWI analysis, the measurements are analysed with the diffusive approximation, as this parameter gives information about the mean free path needed for CWI window design. For these calculations the girder is approximated by a thin slab of infinite lateral extent. Therefore, the calculation is reduced to a two dimensional problem. This is a strong simplification which is mainly caused by two reasons. First of all, while there is an analytic solution for the case of cubic geometries, a solution to the geometry of the I-profile girders is very complex. The other main reason is that the only solution where it is possible to do a linear fit to the data is given by the solution for the infinite body. All other solutions require a non-linear fit for calculation of the diffusivity (D) and the other parameters, which is time consuming. An application for monitoring should be quick and easy (regarding geometry) and therefore I think that in the scope of this thesis, it is reasonable to calculate the diffusivity with the linear approximation described in chapter 2.3.4.

4.1.1 Spectral Energy Density

The diffusivity is calculated by linear fitting as explained in section 2.3.4. For this purpose, the spectral energy density $E(\mathbf{r}, t, f)$ has to be calculated from the measured data. The spectral energy density is time and frequency dependent. The radius r is the source-receiver distance. In order to calculate the spectral energy density the following steps have to be taken (following Weaver (1998) and Deroo (2009)):

- Split the recorded signal into overlapping short windows and multiply those windows with a Hanning window to smooth the edges.
- Transform the data to the time-frequency domain by applying a discrete-time Fourier transformation to every time window and square the results. The result is the so-called power spectral density, which shows the power of the signal at different times. The time corresponding to each window is the center time of the window itself.

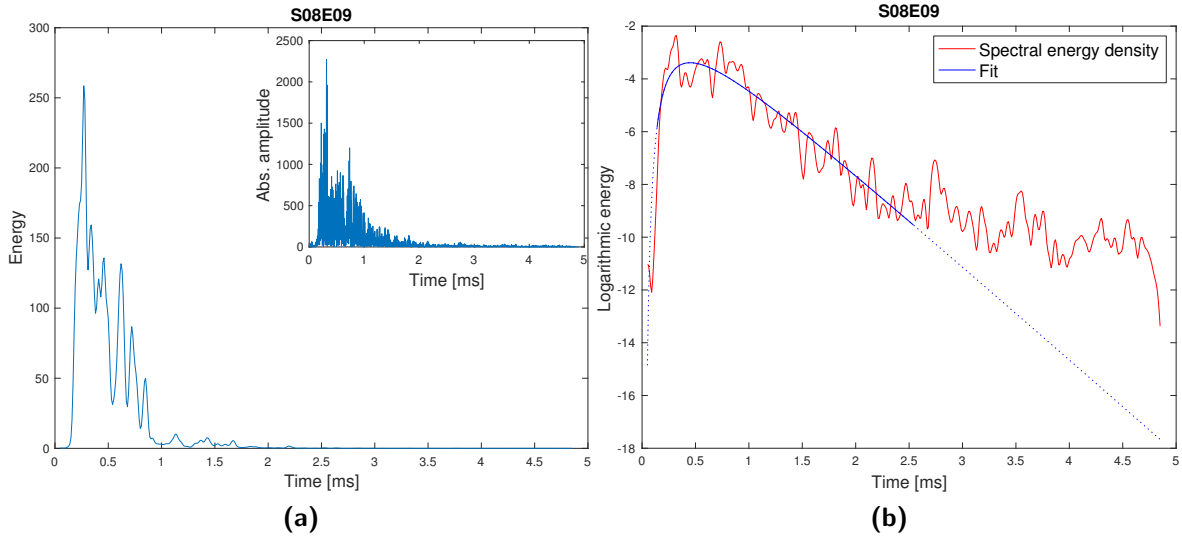

Figure 4.1: The energy spectral density on the left has a similar shape as the absolute amplitude of the recorded waveform. On a logarithmic scale, the solution of the diffusivity equation can be evaluated and displayed (right). Only parts of the energy containing signal energy are used to avoid fitting the noise. The calculated values are $D = 85$ $\frac{\text{m}^2}{\text{s}}$ and $\sigma = 3600$ $\frac{1}{\text{s}}$ in this example.

- To calculate the spectral energy density on a frequency band of length Δf around a central frequency f_c, the power spectral density has to be integrated over this frequency range for every time window.

It is important to note that the spectral energy density calculated here is not the real ultrasound spectral energy density, as it is limited by receiver sensitivity. Nevertheless, it is related with a unknown but presumably constant factor (Weaver, 1998).

According to the US-measurement parameters shown in section 3.3.1, the central frequency is chosen to be 60 kHz. The bandwidth is set to $\Delta f = 110$ kHz to cover the possible signal frequencies. The calculated coefficients A, B and C from equation 2.10 can be directly transformed to the physical parameters. The factor A, including the source intensity P_0, has little absolute meaning due to the previously explained difference between calculated and real spectral energy density.

Figure 4.1(a) shows the spectral energy density for the first measurement of S08E09 in DLT 1.3. As expected, almost all energy is located in the first part of the signal. Compared to the absolute amplitudes of the signal shown in the top right corner, the general shape is similar. In fact, the envelope of the recorded waveform is used for the calculation of the parameters quite often (see (Fröjd, 2018)). As most energy is focused in the first 0.2 ms - 2 ms of the signal, the diffusivity calculations are limited to this part, as the later energy is mostly noise.

With $E(\mathbf{r}, t, f)$ calculated, the linear system of equations in formula 2.10 can be solved and the diffusivity D and dissipation rate σ can be calculated. Figure 4.1(b) shows the resulting diffusivity fit. Only energy from the first half has been used for the fit. The predicted continuation of the fit is shown in dotted lines. While the diffusivity has a big influence

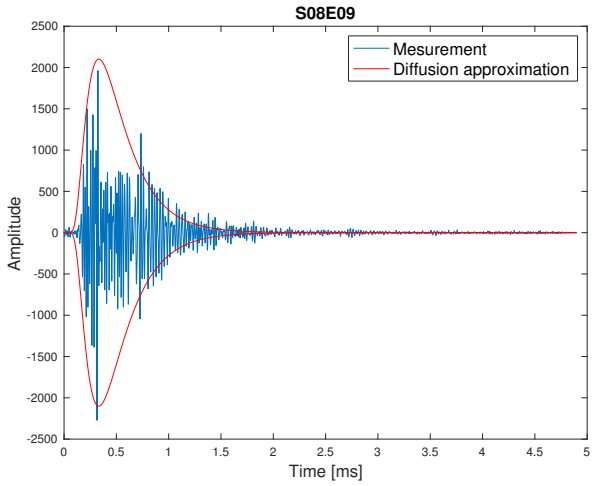

Figure 4.2: The calculated parameters D and σ can be used to plot the solution compared to the recorded waveform. The diffusion approximation encloses the recorded waveform like an envelope.

on the first part of the fit, the dissipation rate σ is dominant in the later part, as D is proportional to $1/t$ in equation 2.10. Therefore, D defines the 'sharpness' of the peak, where the peak becomes sharper with increasing diffusivity and σ defines the slope of the 'tail'.

When transforming back to the signal domain, the diffusive envelope can be calculated for the recorded waveform. This is shown in figure 4.2, calculated using equation 2.8. The first part including the initial signal intensity has to be scaled for the diffusion envelope to fit the signal due to the aforementioned receiver sensitivity issues.

4.1.2 Diffusivity in Girder DLT 1.3

The diffusivity is calculated for every US measurement in the experiment. The starting point for the linear fit is chosen corresponding to the energy level to ensure that only signal energy and not noise energy is included into the calculation. This starting point varies for every source-receiver pair, as the signal starts at different times due to varying source-receiver distances. The average starting time for the window used for diffusivity calculation is approximately 0.2 ms and the end is always set to 2.5 ms to exclude the noise in the late part of the recording. The Hanning window length is set to 0.1 ms and an overlap of 90 % is used.

Figure 4.3 shows the results for the three sensor pairs S07E19, S07E08 and S08E09, which are neighbouring sensors in the middle of the specimen to imitate the approximated geometry of a two dimensional infinite slab. The results are plotted versus the applied load. The calculated diffusivity is between 80 $\frac{\mathrm{m}^2}{\mathrm{s}}$ and 100 $\frac{\mathrm{m}^2}{\mathrm{s}}$. At first, with increasing load, the results stay constant or even increase. Cracks in the specimen should decrease the diffusivity, as they increase scattering and slow down energy spreading through the concrete. S07E19 is the sensor combination closest to one of the areas where cracking starts. Indeed, the diffusivity decreases starting at a load of approximately 800 kN. At this point of the experiment, the specimen already showed numerous cracks on the surface. Therefore, the notch at 600 kN

-700 kN load can be a first damage indicator. The neighbouring combination S07E08 which should sense cracks a little bit later has a notch at 800 kN. At 1000 kN, the diffusivity is further decreasing like for S07E19. For S08E09 no significant decrease is observed, in fact the results are strongly oscillating. S08E09 is located in the middle of the observed area, where cracks on the surface were only recorded at very high loads shortly before failure.

All three graphs show a sudden increase of diffusivity at around 1500 kN. At this point in the experiment the pre-stress was increased to prevent failure. An increase in pre-stress, which is counteracting the tensional strain, closes existing gaps. Therefore, the diffusivity should increase as well. For all three measurements the diffusivity increases back to its initial level (or slightly above that) at the point of increased pre-stress.

Even if the different source-receiver distance was accounted for by different starting times for the diffusivity calculation, the results still show a strong trend with increasing distance. This is illustrated in figure 4.4 at a stage where no load is applied yet. Furthermore, one can see that the diffusivity is varying strongly. While there is an accumulation of results around 80-100 $\frac{\mathrm{m}^2}{\mathrm{s}}$, there are many higher values for all different source-receiver distances. This might on the one hand be influenced by source-receiver distance and coupling issues, but certainly the geometry simplifications play a significant role as well, especially for the sensors located on the top and bottom in the I-profile of the girder. Nevertheless, also sensor pair S09E10 located in the middle of the specimen shows a slightly increased diffusivity value. Similarly, S10E11 looks like an outlier as well but this is one of the sensor pairs with a big source-receiver distance.

Assuming a mean diffusivity of 80 - 100 $\frac{\mathrm{m}^2}{\mathrm{s}}$ for most measurements, the transport mean free path at a shear wave velocity of 2500 $\frac{\mathrm{m}}{\mathrm{s}}$ is 0.064 - 0.08 m or 0.026 - 0.032 ms. Meaning that after this distance/time the distance of US propagation will have changed and the movement gets randomised.

The dissipation rate σ which is calculated simultaneously with the diffusivity is around 2800 $\frac{1}{\mathrm{s}}$ with a standard deviation of around 300 $\frac{1}{\mathrm{s}}$ at zero load. Therefore, the dissipation value calculated in the example shown in figure 4.1 is strongly deviating from the mean and shows the high spread in the calculated sigma values. With increasing load this value is changing in ranges between 2500 and 3200 $\frac{1}{\mathrm{s}}$, but not following a general trend.

4.2 CWI

4.2.1 DLT 1.3

With a mean diffusivity of 80 - 100 $\frac{\mathrm{m}^2}{\mathrm{s}}$ the transport mean free time is 0.026 - 0.032 ms, so the time window for CWI calculation should not start before 0.3 - 0.4 ms. In this way, the time of flight (approximately 0.2 ms), as well as several transport mean free times have passed until the window starts, as suggested by Fröjd (2018). If the coda is still clearly above the noise level, even a later starting time can be chosen to exclude boundary reflections and prominent surface waves.

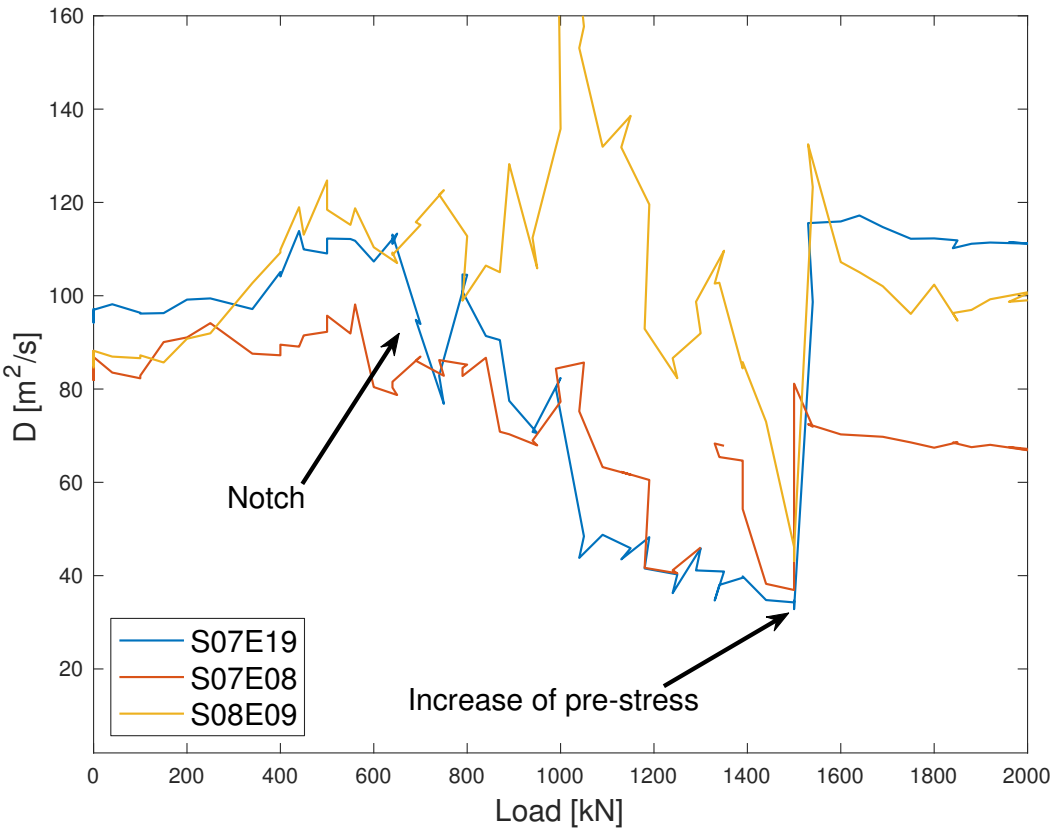

Figure 4.3: The diffusivity calculated with using three different source-receiver combinations starts at a value of around 80-100 $\frac{m^2}{s}$. The sensor pairs S07E19 and S07E08 show a decrease in diffusivity, when cracks are recorded on the surface of the specimen. S08E09 does not show a specific trend. At the time the pre-stress is increased in the experiment, the diffusivity increases for all three sensors.

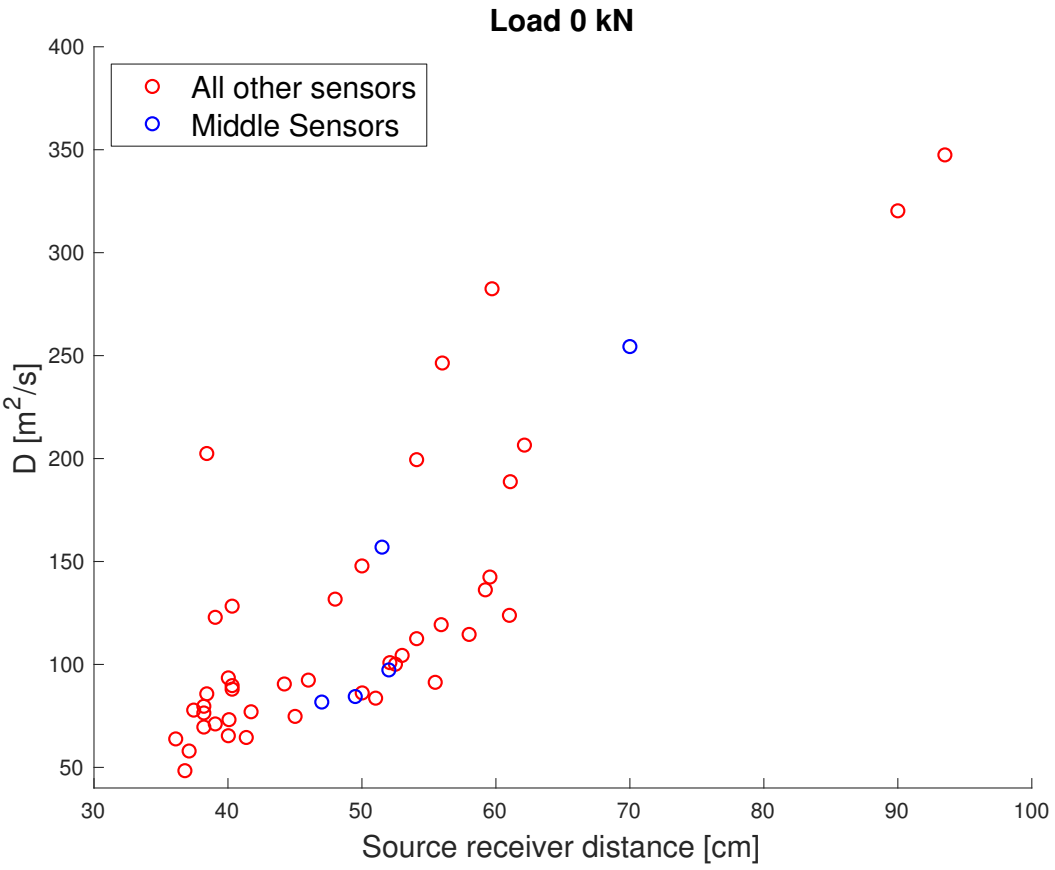

Figure 4.4: The calculated diffusivity seems to slightly depend on the source-receiver distance, even if the different times of flight were accounted for in the calculation procedure. Overall, there is a big deviation in calculated diffusivity. This phenomenon is also evident in the sensor pairs located in the middle of the specimen (indicated by blue circles).

CWI Window Length

Figure 4.5 shows the results of the CWI stretching technique with the standard fixed reference and the stepwise method for different window lengths but the same starting points. The velocity change is plotted over the applied load (in kN). One can see that for all window lengths the calculated velocity changes are similar for each method. At a certain load (or damage level), as already mentioned in chapter 2.4.3, the fixed reference technique becomes unstable and produces oscillatory results, while the stepwise method remains stable. Even past that point the results using different window lengths are similar. Therefore, one can conclude that the length of the window is not a crucial parameter for the calculation, as long as the windows are sufficiently long. It is important to note that all windows ended before the part of the signal which is completely dominated by noise, as random noise should obviously not included in the calculation of the cross correlation.

As shown in figure 4.6, the starting point of the window does also not affect the results in the first time steps significantly where loading is still low and the material changes are not expected to be too big. As soon as the fixed reference method becomes unstable, the results become oscillatory and appear to be completely random. Only the latest starting time at 1 ms greatly deviates from the other results. This observations are similar for the stepwise method, where the latest starting point produces a completely different result as well. Nevertheless, for all other starting times, the results of the stepwise CWI method are pretty stable and similar, also after the point when the fixed reference CWI fails. Therefore, the most crucial point in selection of the starting window is that the window does not start too late, to still include enough signal. Nevertheless, the starting point should be late enough, as mentioned before, to ensure that reasonably much scattering has occurred.

As up till now only the resulting velocity changes have been compared, for completeness, figure 4.7 shows the results from the same tests as in figure 4.5 and 4.6, but this time plotting the correlation coefficient. These results can only be shown for the fixed reference CWI, as a cumulative calculation is not possible for the stepwise method (see chapter 2.4.3). The results are similar to the ones discussed for the velocity changes. One can see that an applied load greater than 800 kN the correlation coefficient gets small in general. This explains the strongly oscillatory results mentioned before, as simply no satisfying velocity change can be found which would produce a good correlation. Looking at the results for different window lengths one can see that the correlation coefficient tends to be larger for shorter windows. The usage of a longer signal in the CWI method includes measurements from a larger area and more scattering events. Therefore, changes in the medium are most certainly included in the long window, but may not be within the shorter windows. Nevertheless, looking at the velocity changes, the physical parameter deducted from this analysis remain similar.

With the given results, the window length was set to a constant amount of 1000 samples (1 ms) for all transducer pairs. The starting point was chosen dependent on the source-receiver distance, as for a longer distance the ballistic waves are expected to be in the later part of the recording. With this set-up it is ensured that the start of the window is several scattering mean free times after the first arrival.

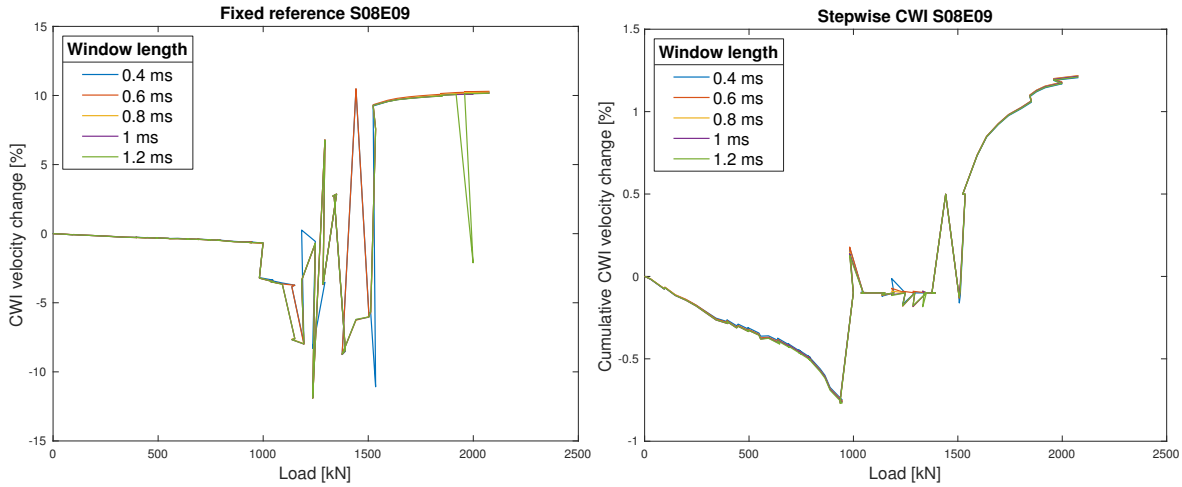

(a) (b)

Figure 4.5: Using different lengths of the time window for the calculation of the velocity change does not seem to affect the result of both methods. The stepwise CWI method is stable for increased load. One should note the differences on the y-axis, as the fixed reference CWI calculates bigger velocity changes in the second half of the experiment.

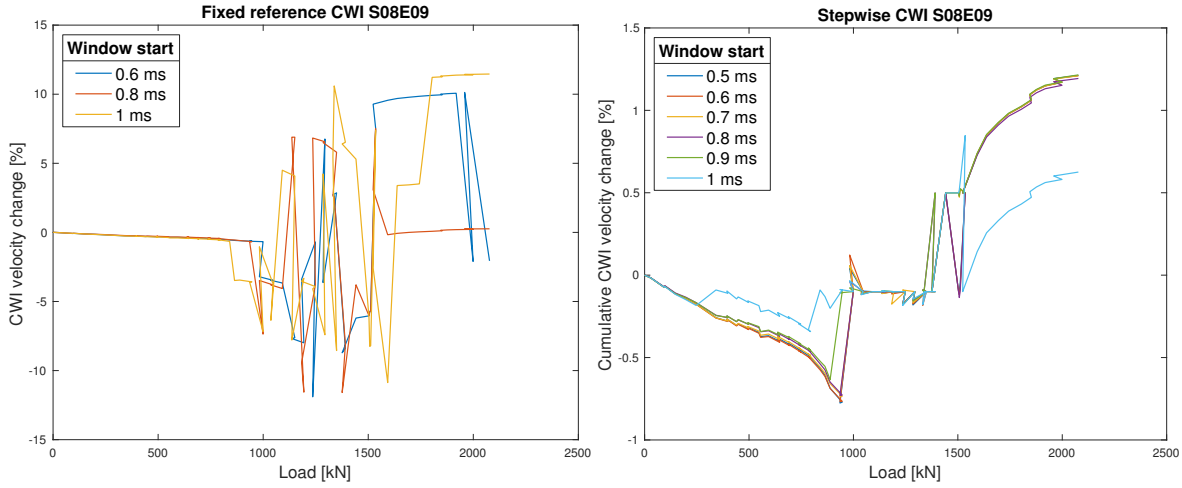

(a) (b)

Figure 4.6: The starting point of the time window does have a bigger influence on the CWI results than the window length. If the window starts late (1 ms), both methods produce a result different to the earlier windows. While the stepwise method again has similar results for all windows in the later part of strong loading and cracking, the fixed reference method produces different oscillatory results. Once again, note the different y-axis scaling when comparing the two plots.

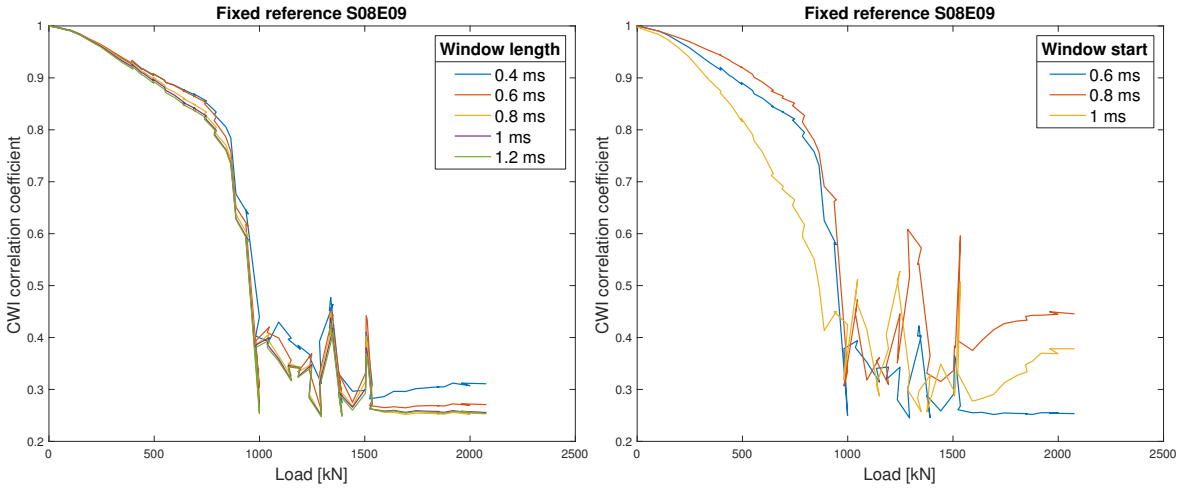

Figure 4.7: The analysis of the corresponding CC coefficient for the fixed reference CWI shows once more, that the window length is not crucial for the outcome. However, the starting point matters.

CWI Analysis at Various Loading Steps

As mentioned in section 3.2.2, the visual damages occurred in a triangular pattern originating from the loading points. With increasing load, the damages propagated to the area between the loading points. Therefore, one can assume that the damages are visible earliest in CWI measurements in the areas of loading. Figure 4.8 shows this behaviour. A general analysis of more source-receiver pairs shows that for both, vertical and horizontal source-receiver pairs, the CWI velocity changes earlier for the sensor pairs closer to the loading point. A comparison with the visual inspections during the loading experiment shows that the indicators from the CWI calculations (strong velocity change) do indeed correspond to the times of damage in this area of the specimen.

For monitoring it is of interest to detect changes in the time before severe damage occurs. Figure 4.9 shows the early phases of loading, where the fixed reference CWI method still produces reasonable results. S10E11, which is the first one showing a drastic response, as it is located in the area of early damage, does not show completely different behaviour compared to the other two combinations. Nevertheless, there is a little notch with a following upwards trend in the phase before the sudden velocity drop. This could be interpreted as an indicator corresponding to a change in the material between both sensors.

The velocity changes from the various transducer pairs in the specimen can be interpolated and plotted on a cross section through the girder. The measurement point for interpolation is the midpoint between both sensors. This method is presented in Niederleithinger et al. (2018). In their paper they show the results of the stepwise CWI stretching technique, while figures 4.10 and 4.11 show the velocity change in the specimen for the fixed reference method at various loading steps. One can see that the velocity changes faster and stronger closer to the loading points. These two areas on the left and right sides of the shown section are the first ones where cracks are visible on the surface. These cracks are indicated in the graphs as

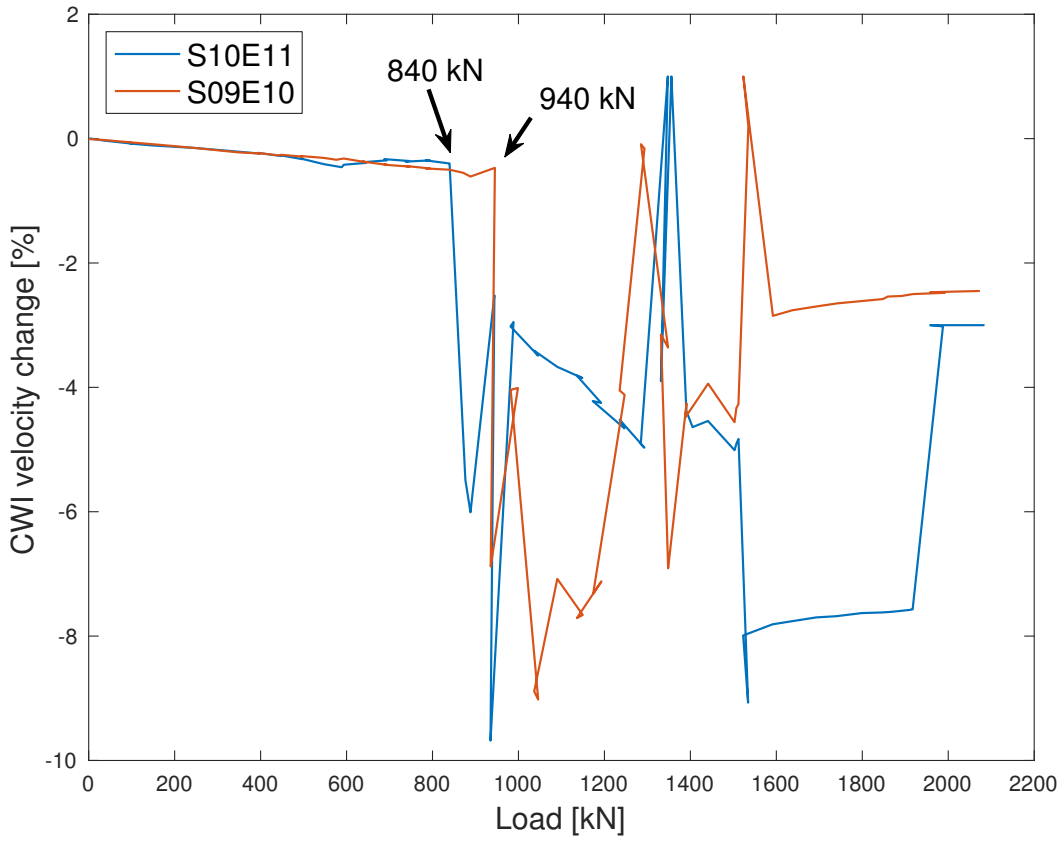

Figure 4.8: The calculated velocity changes show a sudden change at a smaller load for the sensor pair S10E11 than for S09E10 (arrows). This drastic change in velocity can be seen as a major change in material properties and as a possible damage indicator. Indeed, S10E11 is in an area where severe cracking is observed earlier than S09E10.

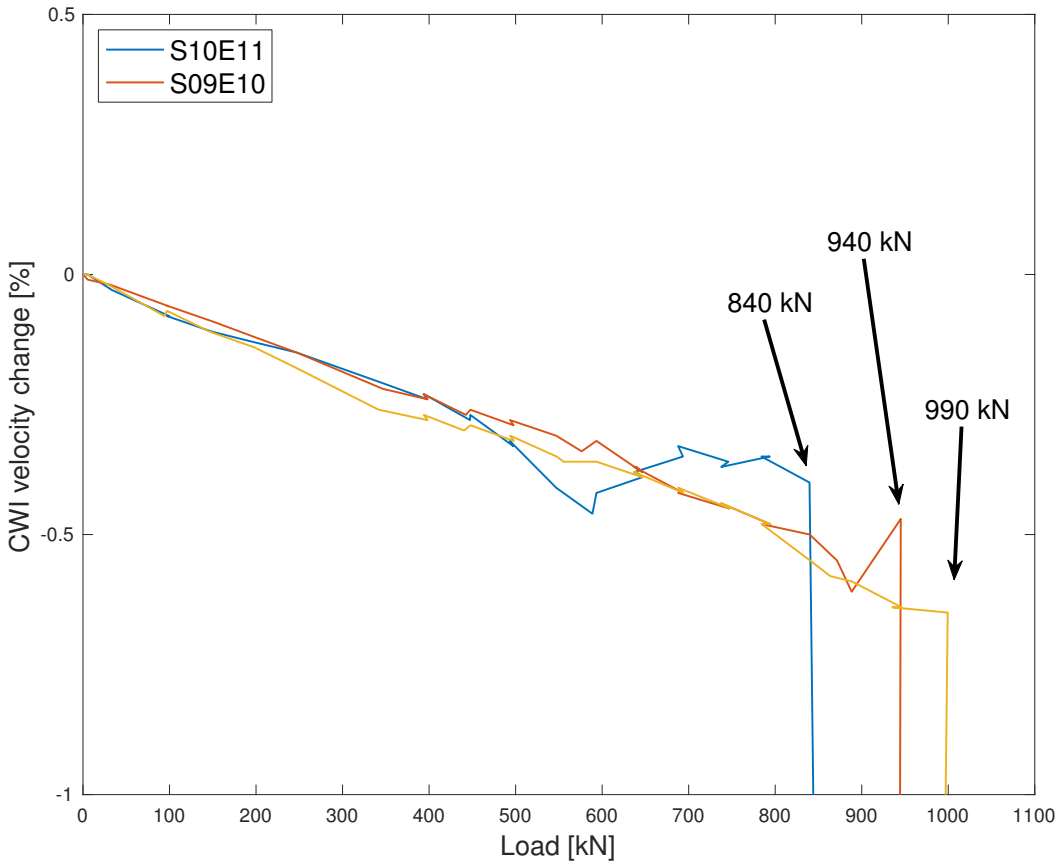

Figure 4.9: Up to a load of 800 kN the velocity is decreasing similarly for all three sensors. S10E11 is responding to damage before the other sensors do (arrows). It even shows a notch at 550 kN followed by a slight velocity increase. This could be related to microcracking or other parameter changes before cracking.

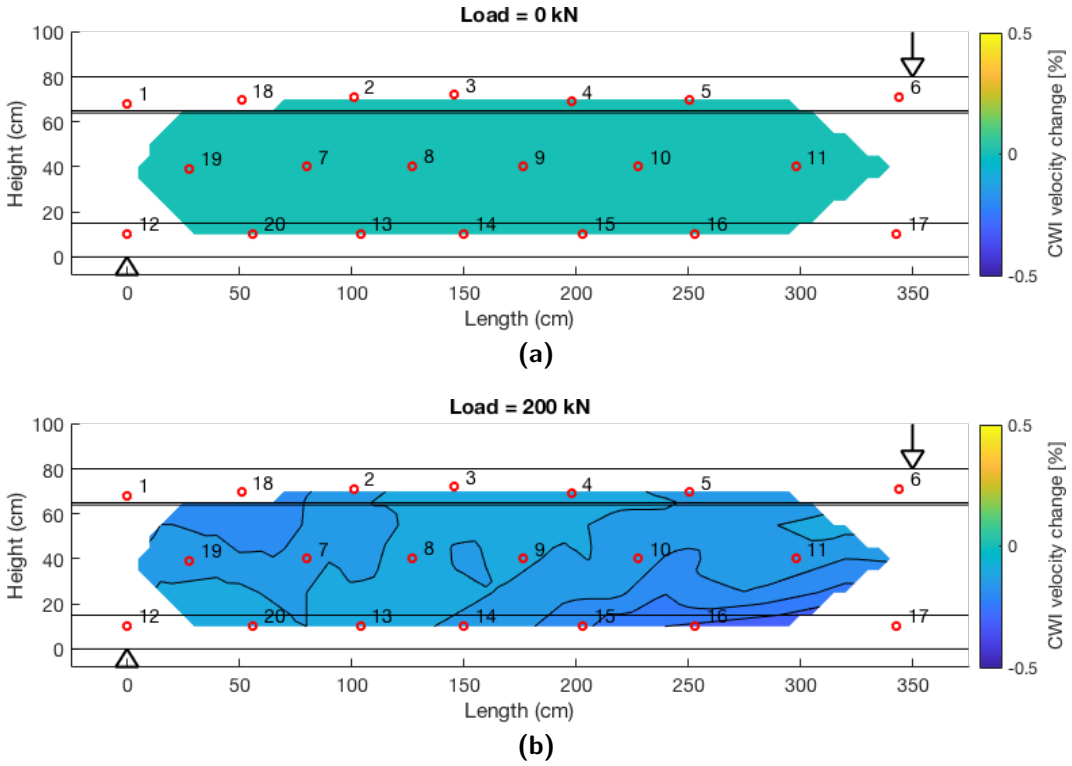

Figure 4.10: For small loads the velocity changes are minimal throughout the whole monitored area. When no load is applied, there is no velocity change (a). At a small load of 200 kN (b) no cracks develop on the girder. Nevertheless, there are already small differences and a slight velocity gradient.

red lines, as soon as they appear.

For small loads, there is almost no velocity change (below 1%). Assuming a shear wave velocity of 2500 $\frac{\text{m}}{\text{s}}$, a velocity change of 1 % corresponds to a change of 25 $\frac{\text{m}}{\text{s}}$. From figure 4.10 (b) one can still see a gradient from almost no velocity change in the center to a minimally bigger velocity change in the areas of the highest tensile stress on the top left and bottom right corner. While for a load of 500 kN first cracks appear on the surface (figure 4.11 (a)), the velocity changes are still below 2% in the sensed area. With increasing load, the velocity changes become bigger. When an increased number of cracks is visible in the areas opposite to the applied load, the velocity changes in this area increase to, or even exceed 10 % (figure 4.11 (b)). At a loading steps close to the failure of the girder (figure 4.11 (c)) the calculated values of velocity change exceed 10 % in many areas and become difficult to interpret due to the previously mentioned unpredictable oscillations. In general, the expected decrease of velocity with increasing numbers of cracks is evident in the shown figures.

Stepwise CWI could help to extend the range of measurements available for analysis. Nevertheless, cracks are already clearly visible at these loading steps and therefore monitoring might no longer be necessary in this area. In the next chapters of analysis, the focus will be on loading stages prior to cracking or at early cracking, as the focus of monitoring is on the elastic part of concrete deformation.

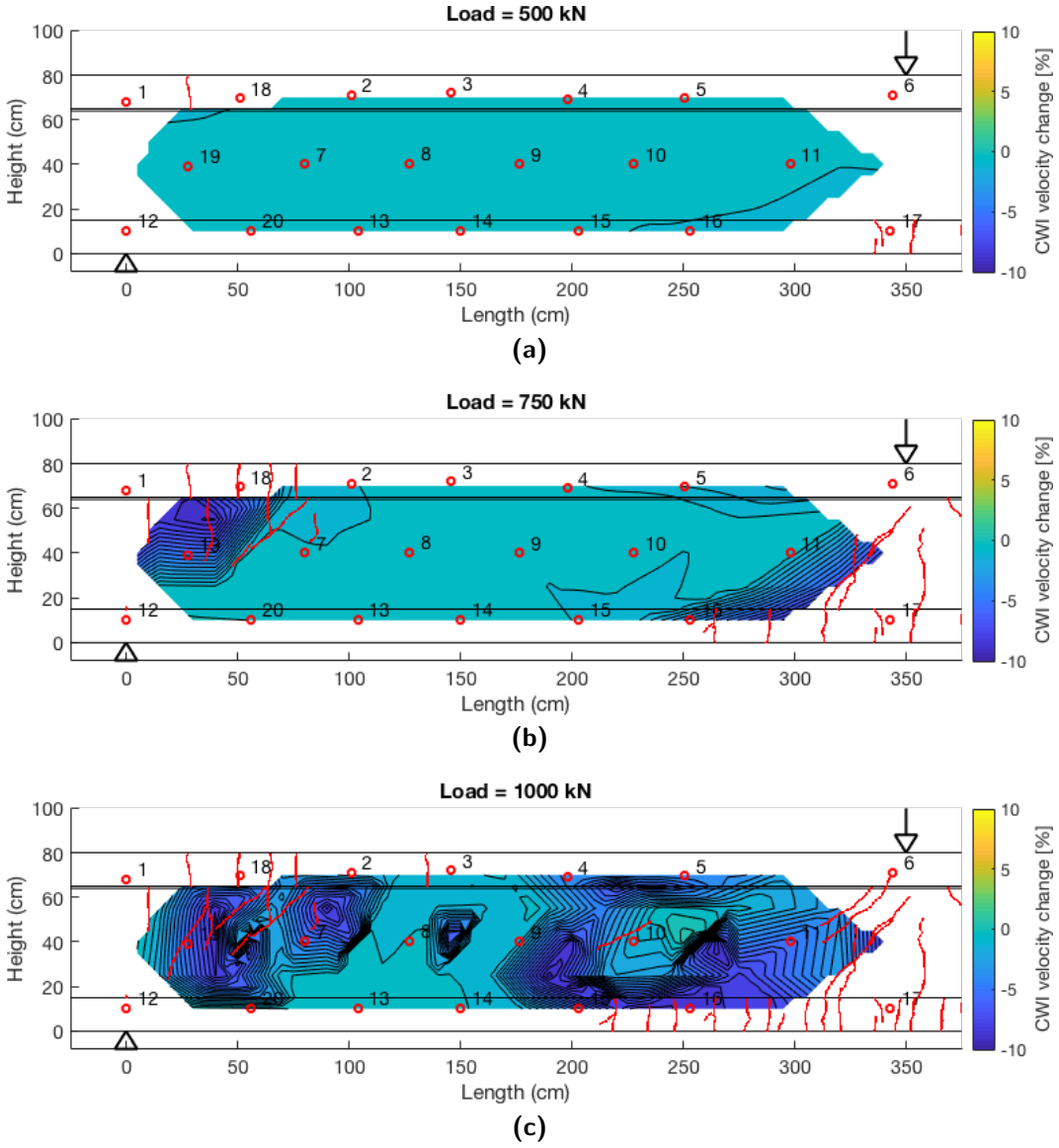

Figure 4.11: At higher loads, the girder starts to show some cracks on the subsurface (a). The velocity decreases stronger in the area closer to the cracks. When the load increases even more, the velocity gradient increases (b). At some point there are velocity drops of over 10 % throughout the girder (c).

4.2.2 DLT 1.5

For girder DLT 1.5 (and girder 1.4) the load is not applied punctually but homogeneously. Therefore, the overall behaviour of velocity change throughout the specimen is different. The selection of the CWI window is similar to the one described for DLT 1.3 using a length of 1 ms, with a starting point depending on the source-receiver distance to exclude ballistic waves. The loading indicated in the maps of velocity change in figures 4.12 and 4.13 is corresponding to the load applied by every single loading cylinder, so the total force on the specimen is bigger than the displayed load. Again, cracks on the surface are indicated by red lines.

One can see that with a homogeneous load, cracking starts earlier. Already at a single barrel load of 30 kN, some small cracks are visible. The velocity in this areas changes stronger than in the apparently undamaged areas. Furthermore, as on the bottom of the girder the tensional strains dominate, while compressional forces dominate on the top, the velocity changes more in the lower parts. At a load of 60 kN, the velocity change in the lower area, where already several cracks are visible is around 4 %. At a load of 90 kN there are already velocity changes of around 10%. The relation between velocity decrease and cracks is evident in these images. For bigger loads the velocity decrease is between 8 % and 10 % , as one can see in figure 4.13(b). Anomalies of only little velocity decrease are also visible. This is evidence for the aforementioned struggles of fixed reference CWI at later loading steps.

In Niederleithinger (2018) and Niederleithinger et al. (2018) it is shown that the stepwise method produces less turbulent images for bigger loads, which is good for interpretation of the general trends. Nevertheless, as the connection of velocity decrease and cracking is well represented in the shown images, crack detection is possible up to a certain time with fixed reference CWI.

4.3 Correlation of Velocity Change and Strain

4.3.1 Small Load Range

The stress-strain relation for concrete is assumed to be linear for small loads as mentioned in section 2.5.2. The concrete strain gauges embedded in the girder record the strains at the point of installation. This measurements can be converted to strains in the two main directions, as shown in section 3.4.2.

The following part of the thesis shows the behaviour of velocity change and strain in the specimen for small loads. As the inductive displacement sensors attached to the girders do not have a resolution fine enough to detect those early changes, only the data from the embedded concrete strain gauges can be used. This limits the available data to only one measurement for girders DLT 1.3 and two for DLT 1.5. In fact, for DLT 1.5 only one strain gauge could be used due to unsatisfactory data from one of the available sensors.

DLT 1.3

As one can see in figure 4.14, there is no transmitter-receiver combination with a midpoint at the location of the concrete strain gauge in the center of the girder section. Therefore,

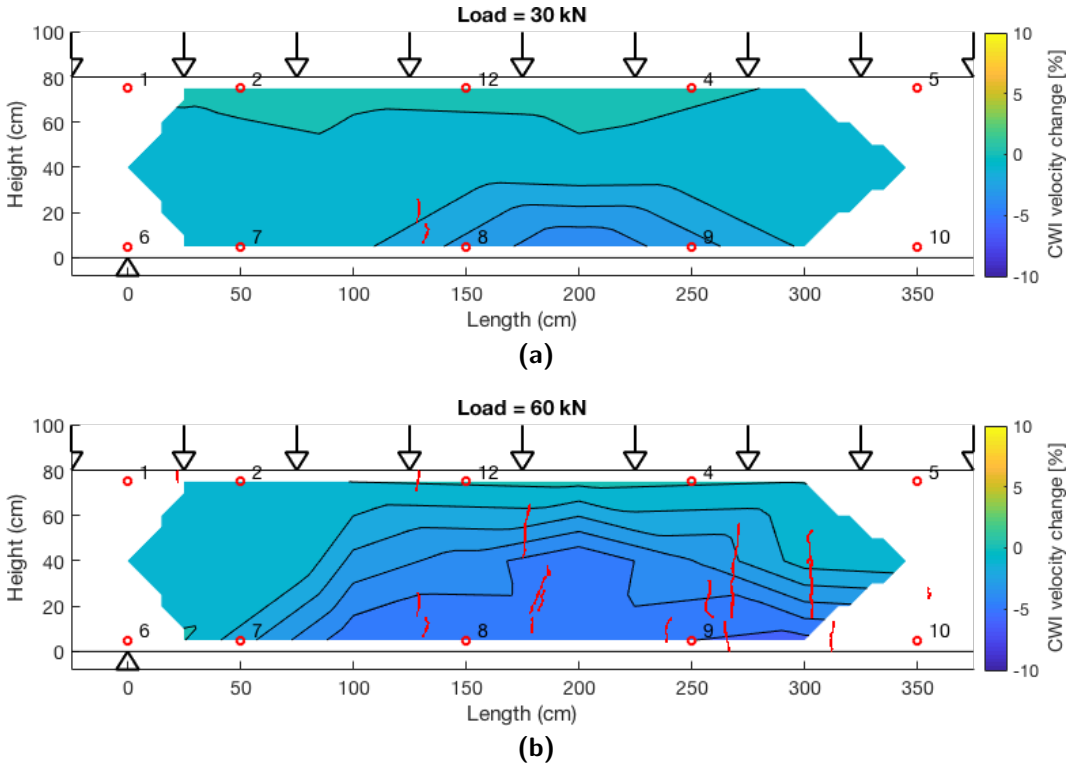

Figure 4.12: The maps of velocity changes for girder DLT 1.5 show that the girder starts cracking at smaller loads already. One must note that this is the load per loading barrel, so the total force is greater than the 30 kN. Even at a load of 30 kN small cracks appear (a). The map shows a velocity decrease in the cracked area. When the load is further increased (b), more cracks develop especially on the bottom of the girder and the velocity decreases.

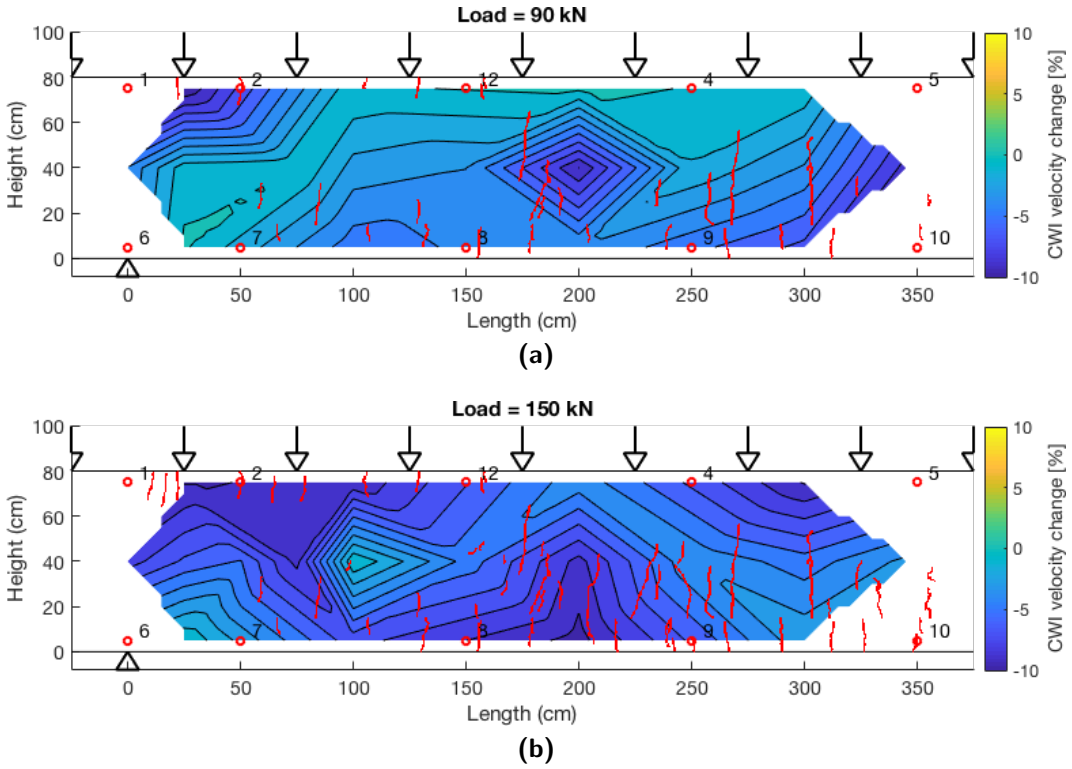

Figure 4.13: On DLT 1.5, starting at a load of 90 kN (a), one can already see velocity changes of more than 10%. At bigger load (b), the fixed reference CWI struggles because of the strongly disturbed concrete.

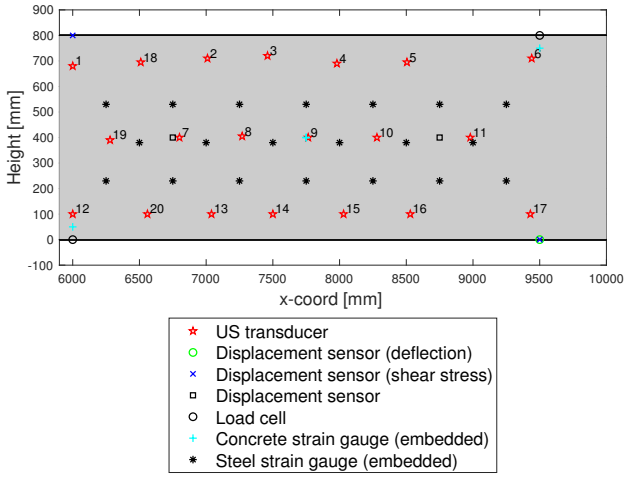

Figure 4.14: Map of all available sensors in DLT 1.3

two measurements are interpolated. ϵ_1 is pointing in a 30° - 35° angle downwards from the horizontal plane (for the calculation of the angle see equation 3.2), thus sensor combination S03E09 and S09E15 is used as these measurements are in the same direction as ϵ_1. This direction is perpendicular to the cracks' directions for bigger loads.

Figure 4.15 shows the comparison of strain and velocity change for the mentioned transducer combination. One can see that both, ϵ_1 and the velocity change are changing linearly for small loads. Both measurements are close to zero for no load. While the velocity is decreasing with increasing load, the tensional strain is increasing. This linear relationship is also evident when comparing velocity change and strain directly, as done in figure 4.16. As the ultrasound measurements were repeated less frequently than the strain measurements, the resolution in the strain images is better. The velocity data is interpolated with respect to the applied load in order to compare strain and velocity change.

This linear dependency can be used to create maps of strain from CWI measurements, like it has been done for the velocity change. Figure 4.17(a) shows a map of strain at a load of 250 kN using only transducer combinations pointing in a similar direction as S03E09 and S09E15. For comparison, figure 4.17(b) shows the results using only horizontally directed transducer combinations. In both maps, the values of ϵ_1 are in a similar range. Furthermore, both maps show an increased strain change in the top left and bottom right corner, which are closest to the areas of maximal tensional strain opposite to the loading points. To calculate the strain at positions other than the concrete strain gauge, simply the ratio of velocity change and strain change (the slope of the linear fit in figure 4.16) is calculated and assumed to be constant throughout the girder. With the velocity changes calculated for many transducer pairs, the areal maps can be created. Such maps do not show more information content than the maps of velocity change, as they are simply scaled versions of these previously shown maps, but might be easier to interpret for people with an engineering background.

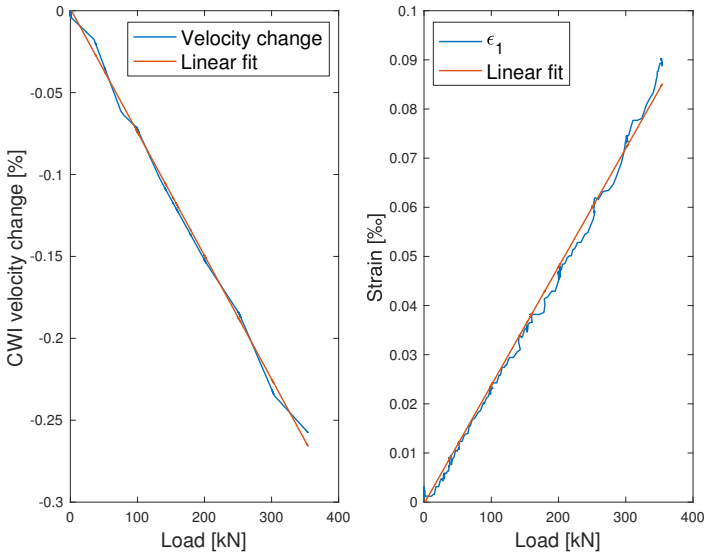

Figure 4.15: The comparison of velocity change recorded by the combinations S03E09 and S09E15 (left) and the strain ϵ_1 both show a linear dependency with respect to the load applied to the girder, given that the load is small. The linear behaviour is illustrated with a linear fit.

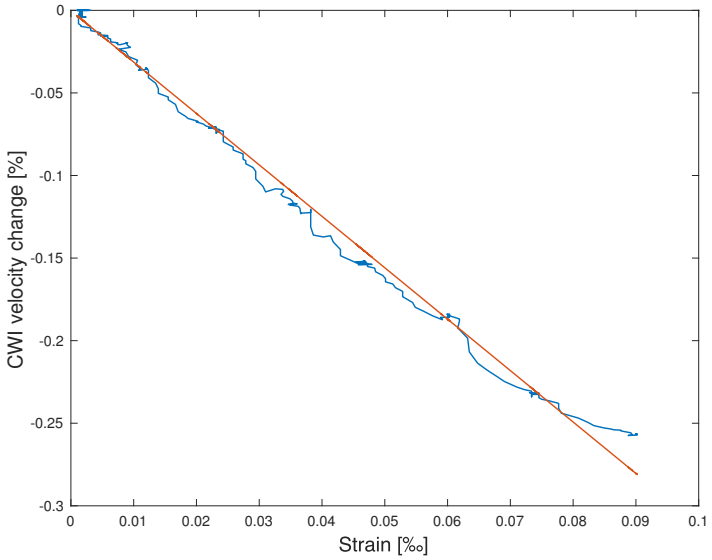

Figure 4.16: The linear behaviour is also given when velocity change of S03E09 and S09E15 is plotted over the strain directly, given that the load is small (< 350 kN). The linear behaviour is illustrated with a linear fit.

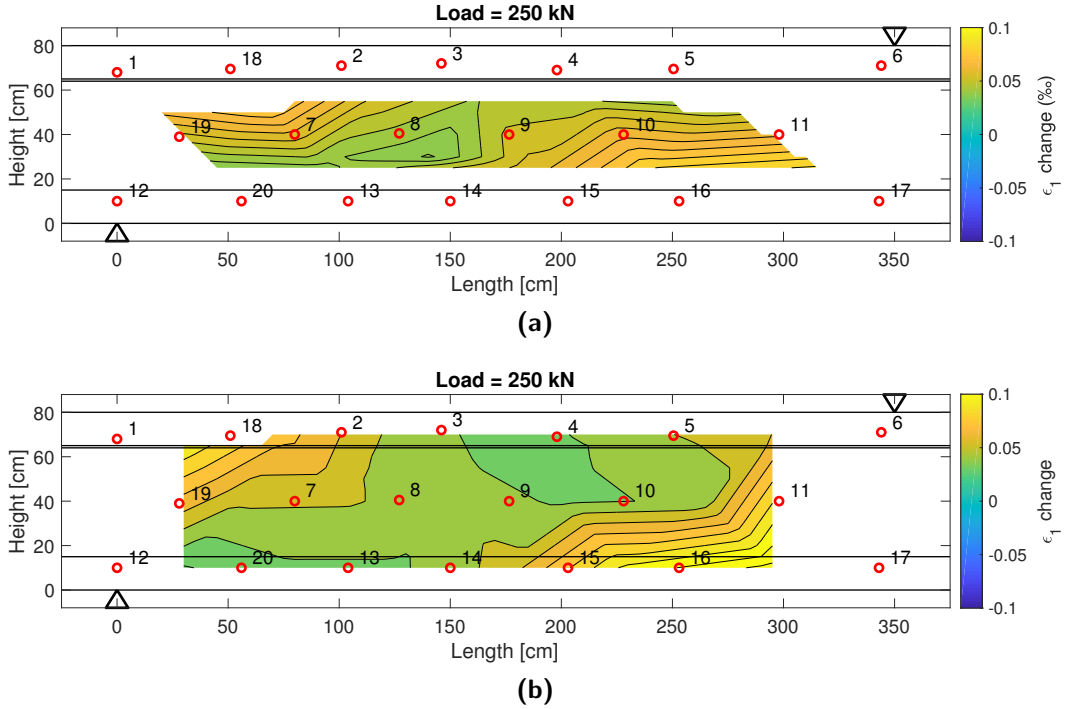

Figure 4.17: The velocity change can be transformed to the relative strain change for small loads by a simple linear relation. Only transducer pairs with similar direction are used. In (a), this is only diagonal transducers (like in figure 4.15) pointing in the direction of ϵ_1 the main strain, in (b) only horizontal transducer pairs are used.

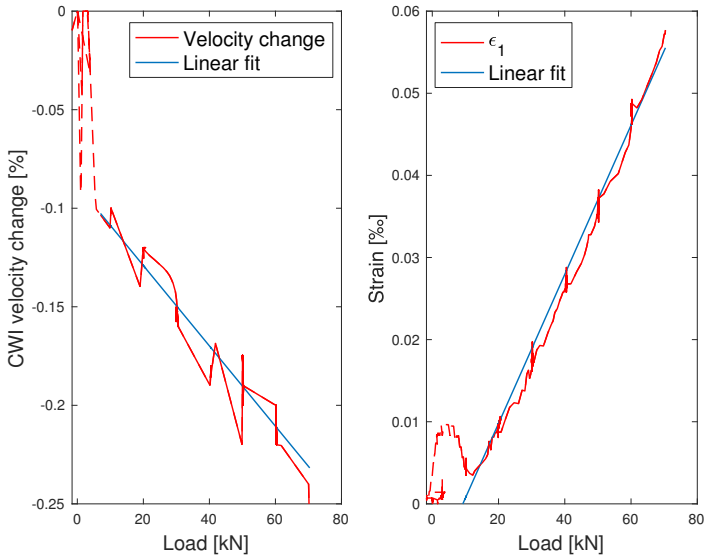

Figure 4.18: Using the concrete strain gauge D4.1 in DLT 1.5 and sensor pair S02E07, the data is plotted versus the applied load. There is a jump in velocity, as well as in strain for loads smaller than 10 kN, which is why the data is fitted from 10 kN onwards. From 10 kN to 65 kN load, both velocity and strain, appear to be constantly changing with increasing load. Nevertheless, there are wiggles, especially in the velocity plot.

DLT 1.5

For the analysis of the early loading phase, the vertical sensor pair S02E07 and the concrete strain gauge D4.1 are used. The results could not be reproduced using other ultrasonic transducers in that area, as they were affected by the early cracking in the specimen, while the results of the CWI analysis for S02E07 remained relatively stable. The main strain direction ϵ_1 is pointing 40° downwards from the horizontal.

Figures 4.18 and 4.19 show velocity and strain during the first phases of loading. There is a drop in velocity change when applying the first load, as well as a peak in strain during this phase. The load measurements show that before the load increase, loads of 3 kN - 7 kN per loading barel were applied inconsistently. The reason is not known. Therefore, the data is plotted between loads of 10 kN and 65 kN. The velocity is decreasing with increasing force, while the strain is increasing.

One can see a linear dependence of both, strain and velocity change, to applied force as well as to each other. Due to the mentioned behaviour at loads smaller 10 kN, the linear regressions to the graphs can not be traced back to zero at zero load. Furthermore, there are spikes and immediate drops in the graphs. In the homogeneous load experiments, the force is applied stepwise, with short breaks, where the force is kept constant. Keeping the load perfectly constant is difficult with the used equipment, so it sometimes decreases slightly in between the loading steps. Hysteresis and creeping might have influenced the velocity profile as well. Nevertheless, linear behaviour can be shown for loads up to 65 kN per loading barrel where the specimen already starts to crack.

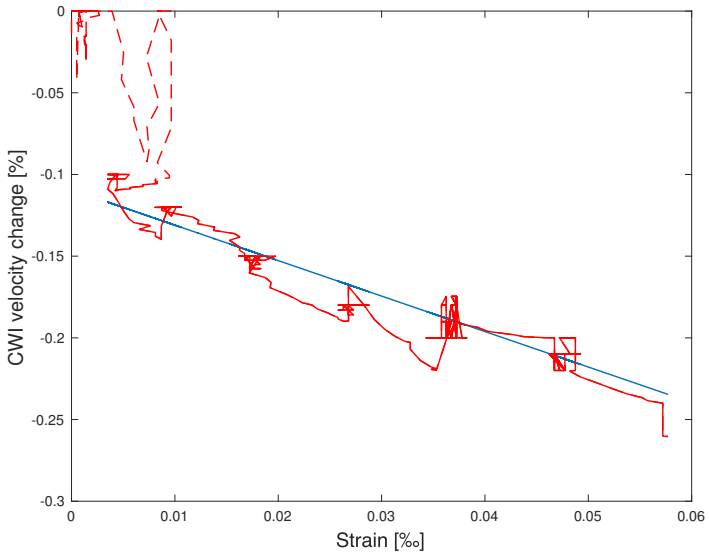

Figure 4.19: The plot of velocity change over strain for loads between 10 kN and 65 kN shows a linear trend. Data from the beginning of the experiment can not be used (dashed line). The spikes are caused by secondary effects during the phase of the load resting on the specimen between stepwise increase.

4.3.2 Small to Medium Load Range

As shown in section 2.5.2, when the load increases, the stress-strain relation can no longer be approximated linearly and Young's modulus is not constant anymore. Therefore, acousto elastic theory with Young's modulus depending on ϵ is applied here for bigger loads. This is first of all an approach to find dependencies between velocity change and strain change for bigger loads. Furthermore, the non-linear parameter β can be approximated from a comparison of stain and velocity change according to Jin et al. (2017). As the strains increase for bigger loads, the inductive displacement sensors can be used for strain calculation as well. One should keep in mind, that the results from the inductive displacement sensors are an average over a large area, so the strains and parameters calculated with their data might be inaccurate when regarding to a single midpoint.

DLT 1.3

In girder DLT 1.3, the embedded concrete strain gauges, as well as inductive displacement sensor R3 can be used. R4, which is also in this area, did not provide good results for the strain, so it will not be analysed here. Figures 4.20 and 4.21 show the velocity change plotted over the strain measurement of the concrete strain gauge and the inductive displacement sensor respectively. As a sufficient amount of ultrasound measurements is available, only those data points are used to avoid the problem of erroneous interpolation. The velocity change is doubled, due to the approximation of Young's modulus explained in section 2.5.2. For the determination of the velocity change, again sensor pairs in the direction of the main strain are analysed. For R3, the main strain ϵ_1 is also pointing downwards from the horizontal in approximately 40°, so data from sensor pairs S07E18 and S07E13 is used for the velocity

values. In figure 4.20 the data is fitted up to a load of 800 kN, while for 4.21 this trend can only be shown up to a load of 700 kN. At bigger loads, the velocity decrease and the strain increase are stronger and no longer following the shown trend.

The stain measurements at the inductive displacement sensors are averaged values over a length of 500 mm per sensor. Therefore, the resulting strains are not as stable and slightly oscillating. For both plots, the general non-linear trend is obvious. The data is fitted with a second degree polynomial according to equation 2.24 in order to determine the non-linear coefficient(s). The results of the fitting process are given in the bottom left corner of the graphs, where coefficient β corresponds to the first order term $\beta\epsilon$. The results differ significantly, which is not surprising, as the strains measured also differ a lot. This is caused by the two different measurement techniques used. It is not known which measurement over- or underestimates the strain, or if even both are inaccurate on an absolute scale.

As shown in figure 4.11, cracking starts at around 500 kN load, so there the deformation is already starting to be non-elastic at this point. The clear trend can be shown for a longer time tough. This means, using the relation of velocity change and stress, an assesment of concrete in the stage of partly inelastic deformation is possible.[1]

When using different transmitter-receiver combinations in the area of the strain sensors, the results for beta are of similar order than the ones shown here. For some transducer pairs, the fitting can not be continued to 700 kN load, as their velocity measurements were already affected by cracks.

DLT 1.5

For girder DLT 1.5, two embedded concrete strain gauges, as well as two inductive displacement sensors were available in the area the US measurements were carried out. The strain measurements of R4 (inductive displacement sensor) and $D4_2$ (embedded) were both in similar locations and did not give satisfying results. For this reason, only R3 and $D4_1$ are used with the corresponding US transducers. The direction of ϵ_1 at both sensors is 40° downwards from the horizontal. For both plots the same velocity measurement (S02E07) could be used, no averaging between two source-receiver combinations had to be done.

The trend of velocity change versus strain shown in figures 4.22 and 4.23 is again well fitted with a second order polynomial, as in the previous section. The relationship remains in this shape up to a load of 110 kN, which is way beyond the load when cracking starts in the specimen. The relation of strain and velocity even shows an upward trend (before failing) in the end for both sensors. Again, the values for the non-linear parameters are given in the figures and differ when comparing the two different strain measurements. Comparing the results from DLT 1.3 and DLT 1.5, the β values for using the embedded sensors differ as well. The values for girder DLT 1.5 are about double the results for 1.3. One must note that the strain levels used for girder 1.5 are smaller than for girder 1.3. The cubic non-linear parameter δ is similar for the inductive displacement sensor, but not for the concrete strain gauge.

[1] It was tried to apply stepwise CWI to ensure stability of the velocity calculation for bigger loads but the results did not improve significantly.

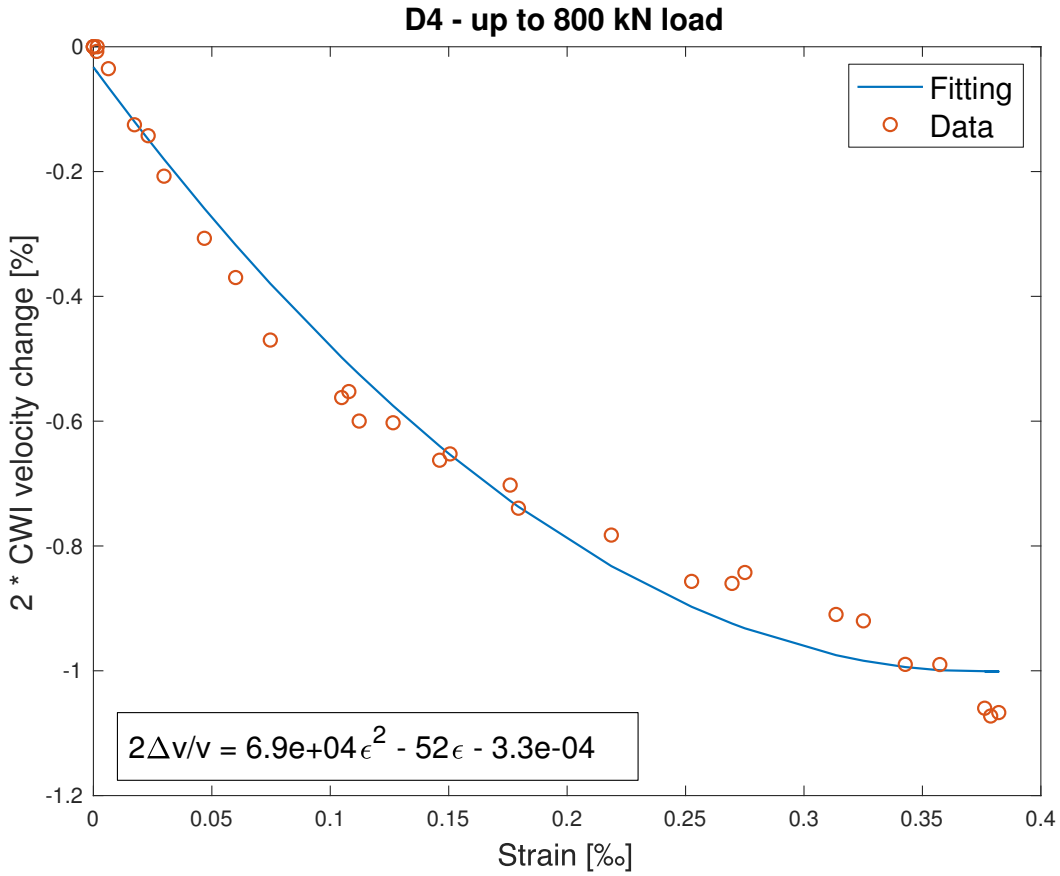

Figure 4.20: The plot of the velocity change (S03E09 and S09E15) over the strain (measured with the concrete strain gauge D4) can be well fitted with a second order polynomial. Only measurements at the time of US measurements were used. The polynomial with its fitted parameters is mathematically given in the bottom left corner. The shown relation holds up to a load of 800 kN.

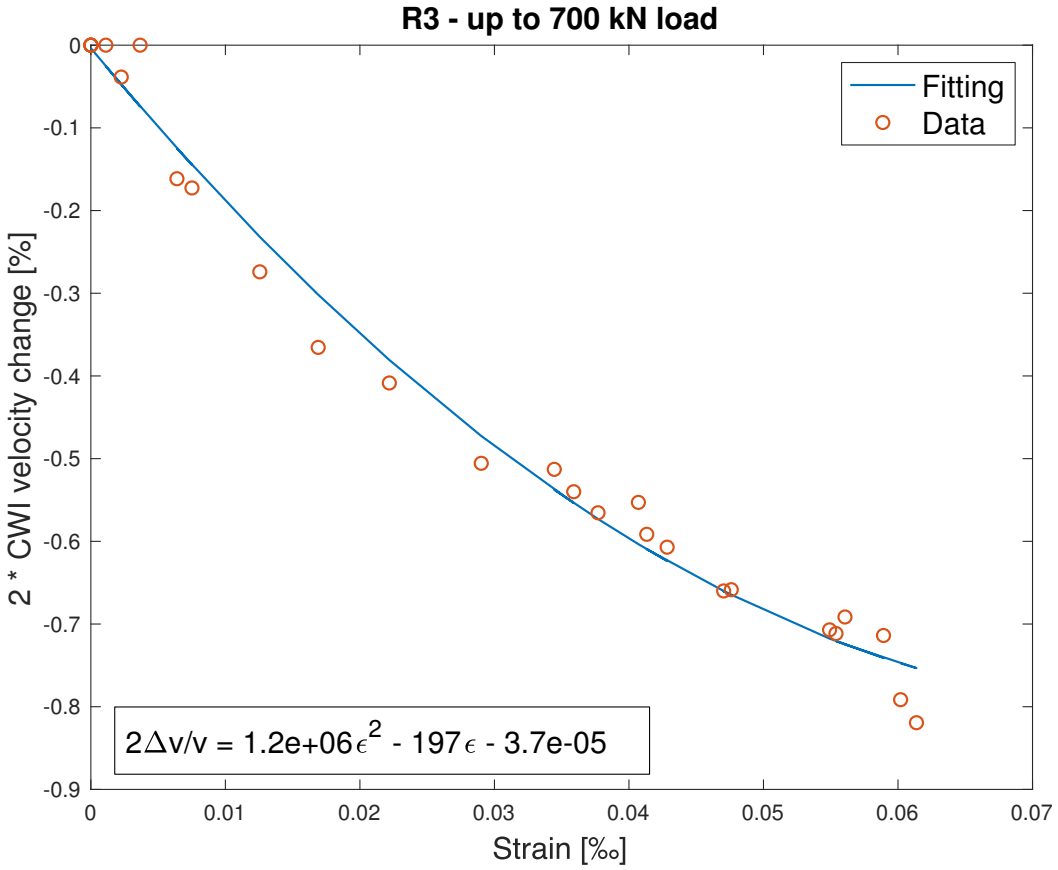

Figure 4.21: Similar to figure 4.20, the plot of the velocity change (S07E18 and S07E13) over the strain (measured with the inductive displacement sensor R3) can be well fitted with a second order polynomial. The polynomial with its fitted parameters is mathematically given in the bottom left corner. The shown relation is holding up to a load of 700 kN.

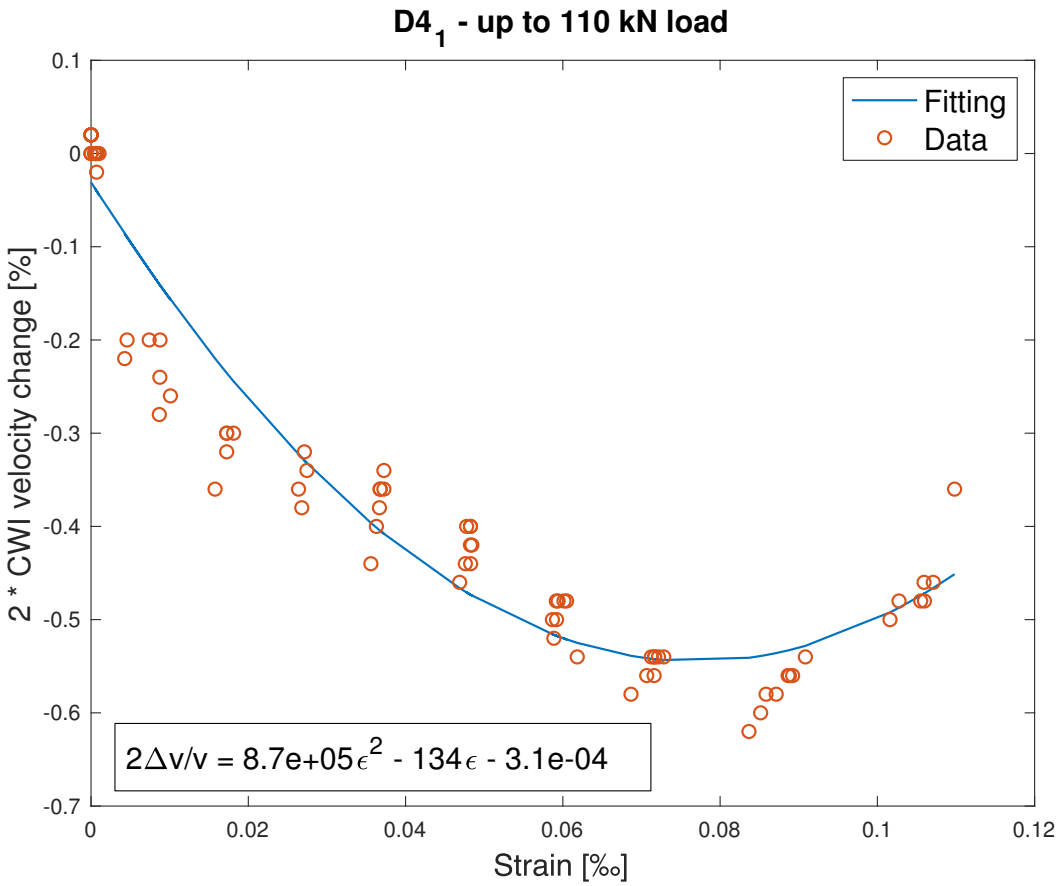

Figure 4.22: For DLT 1.5, the relationship between strain (concrete) and velocity change follows a similar trend as for DLT 1.3. It is fitted with a second degree polynomial, giving the values for the non-linear constants β and δ.

The graphs in figures 4.22 and 4.23 show an accumulation of measurement points at certain strain level, where the velocity change decreases slightly. The reasons for this behaviour are similar to the ones explained in 4.3.1. In the phases the load is kept constant, a mixture of secondary effects causes changes in material parameters which influence the ultrasound measurement. One reason might be hysteresis, which is not discussed within this thesis. Further information on experiments on hysteresis with ultrasound can be found in Payan et al. (2010). As for DLT 1.3, it was not possible to use other velocity measurements in that area up to a load of 110 kN, as their measurements were most likely affected by cracks.

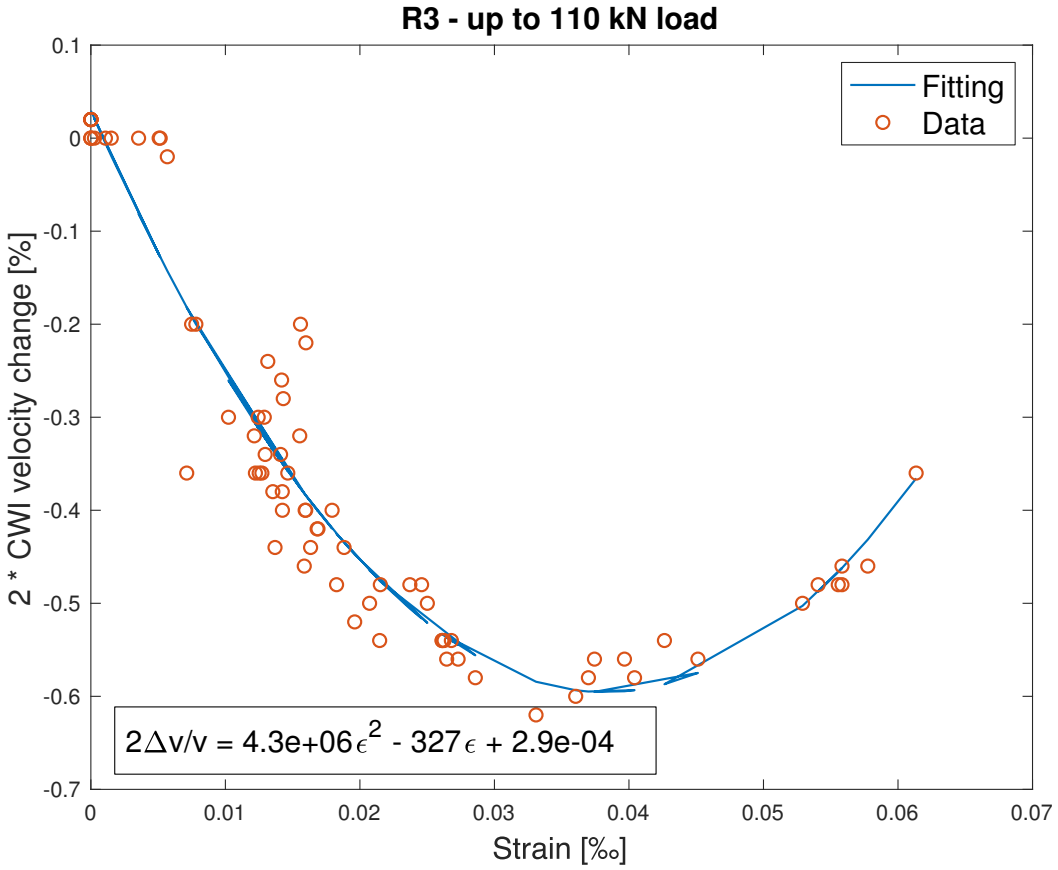

Figure 4.23: Using the stain measurements from the inductive displacement sensors, the second order polynomial fit works well for DLT 1.5. The unsteadiness in the polynomial is caused by strain drops happening throughout the experiment in the phases of constant loads.

Chapter 5

Discussion

The presented results will be discussed in the following sections, beginning with the diffusivity, followed by the CWI analysis and concluded by the combined analysis of US and strain measurements. If possible, the results are compared to findings in current literature.

5.1 Diffusivity

It has been shown in section 4.1, that the measured ultrasonic data can be used to calculate the spectral energy density. The spreading of energy can be described by the decay of energy measured with the receiver. Using the model of a two dimensional infinite plate, this decay can be described with a linear approximation if the energy is plotted logarithmically and a coefficient called diffusivity is calculated.

The results for the diffusivity parameter range from 50 to 300 $\frac{\mathrm{m}^2}{\mathrm{s}}$ for measurements at zero load, but mostly the diffusivity is between 70 and 100 $\frac{\mathrm{m}^2}{\mathrm{s}}$. The dissipation rate is strongly varying with a mean of around 2800 $\frac{1}{\mathrm{s}}$ and a standard deviation of 300 $\frac{1}{\mathrm{s}}$. A comparison of the different transducer combinations shows the problem of different distances of source-receiver. The first break is at different times, which has to be included into the selection of the time window of the energy fitting process. Nevertheless, the data still shows a trend of higher diffusivity at bigger source-receiver distance. At a center frequency of 60 kHz, which has been used in the experiments, we are still at the boundary between simple and multiple scattering regime in the used concrete. A significant part of the energy is in the ballistic waves at the beginning of the signal. When the source-receiver offset gets bigger, the ratio between ballistic wave energy and multiply scattered coda energy in the late part of the signal is bigger than for short offsets. Therefore, the energy spectrum shows a strong spike in the first section with a quick decay. Using the diffusive approximation, this is interpreted as fast energy spreading and results in a high diffusivity value. This shows that at frequencies in the simple scattering regime, the diffusive approximation is not perfectly describing the wave propagation, as the source-receiver distance influences the results.

Taking this into account, as well as regarding to the measurements above 150 $\frac{m^2}{s}$ as outliers, the values for diffusivity are in an acceptable range, considering that the calculation was done with a strong simplification of the geometry. In literature, mostly higher frequency transducers are used in diffusivity analysis, as they aim for the multiple scattering regime. Fröjd and Ulriksen (2017) have investigated CWI for different frequencies ranging from 3.1 kHz to 500 kHz. Within their study they also investigated both scattering parameters D and σ (dissipation rate) with a more sophisticated solution of the diffusion equation using the geometry of a finite 3D cuboid structure. The calculation of the values was done with a non-linear least square fit. For a frequency of 50 kHz they calcualted a diffusivity of 440 $\frac{m^2}{s}$ and a dissipation rate of 1200 $\frac{1}{s}$. The next higher frequency they used was 150 kHz, with values of 39 $\frac{m^2}{s}$ and 7000 $\frac{1}{s}$. The diffusivity in an intact concrete structure depends on material parameters, as the composition of concrete allways differs. Nevertheless, a general comparison of calculated and reported values is meaningful. The values from Fröjd and Ulriksen (2017) are bigger for the 50 kHz measurement diffusivity and smaller for the dissipation rate compared to the values in this thesis. For higher frequencies, the diffusivity strongly decreases, while the dissipation rate strongly increases. Taking differences caused by both, concrete parameters and difference in frequency, into account, the values calculated in this thesis seem reasonable. Furthermore, the experiment on the bridge girders was not specifically designed for this analysis, while the experiment from Fröjd and Ulriksen (2017) was specially designed for US parameter analysis. During concreting, transducer positions might have changed slightly, coupling can vary and other sensor specific factors might influence the recording and therefore the diffusivity results. This can be seen as an explanation for the strong variations of diffusivity in figure 4.4.

Cracks are expected to decrease the diffusivity. Sensors which were in areas of cracking indeed showed a strong decrease in diffusivity at increasing load. Even the increase in pre-stress can be seen in the plots, as diffusivity increases at that time. Therefore, the diffusivity seems to be senistive to damage. Nevertheless, the diffusivity analysis does not show an earlier response to damage as CWI does. Furthermore, due to the varying values, it is difficult to interpret and therefore only of limited interest for monitoring itself.

The dissipation rate did not show a trend with increasing load and cracking, which is expected, as the energy decay is caused by intrinsic scattering (Fröjd and Ulriksen, 2017)

The diffusivity is an important parameter for modelling and inversion (see Larose et al. (2010) and Rossetto et al. (2011)). It is also a good supportive tool for experimental parameters like source-receiver distance (scattering mean free path) or CWI window length. Therefore, in the scope of this thesis, I suggest that diffusivity analysis is used in the planning phase of bridge monitoring tasks, to ensure a good experiment setup.

5.2 CWI

For the calculation of the CWI velocity change, the used time window of the signal is a crucial parameter. It is important to include relevant coda and exclude noise, as its randomness will decrease the CC coefficient. It has been shown, that for both methods, the starting point of the CWI window matters, while the window length does not significantly influence the result. Showing that the window length does not affect the result supports the claim in Planès and Larose (2013) that the stretching method can use bigger windows, unlike the doublet

technique, where short windows are required. Nevertheless, it is important to start the window reasonably early. The signal strength decreases with time, as scattering attenuates the signal. The decreased signal-to-noise ratio does influence the CWI, as the noise has a stronger influence on the signal shape in the later parts. As long as the CWI window starts early enough, the results are similar.

Comparing stepwise and fixed reference CWI, the stepwise method is less affected by window parameters than the fixed reference CWI in the later times of the experiment. This is expected of the stepwise method, as changes between two following recordings are generally not that big, except major cracks appear in between two measurements. Nevertheless, at the stage where the fixed reference CWI fails, there are already cracks visible on the surface. Before that, both methods produce similar results and are therefore equivalent for smaller loads. Furthermore, using the fixed reference CWI, changes in the material produce steeper velocity gradients, as the differences between the recorded signals are bigger. This might be easier to interpret or detect automatically with regard to monitoring. When changes are detected, the data can be re-evaluated manually and both methods can be used. The loads in the experiment increase drastically within a short time, which is unlikely to happen for most bridges in reality. Therefore, I expect monitoring tasks to mainly operate in the elastic domain of concrete deformation where the fixed reference method produces perfectly fine results. As this method is computationally faster as well, I advice usage of the fixed reference method for fast analysis.

The maps of velocity change are a good tool for evaluation of big structures. They show good correspondence with cracking patterns for both girders. In the single load experiment, one can clearly see that the extensively strained areas are showing the by far biggest velocity change. Even if the ultrasonic transducers embedded in the specimen did mainly cover the area in between the loading zones, the damages can be detected on the edges of the sensed area. Already at smaller loads ($\leq$ 500 kN), where only minor cracks appear, there are velocity gradients visible and give a good image of the stress-strain changes in the girder. With extensive cracking, anomalies appear in the map, where the velocity change gets too big. This can be reduced when switching to the stepwise method. Therefore, this method is favourable, when some areas are known to be damaged, while others are still expected to be intact. Maps created with the stepwise method will then be better for interpretation, as strong anomalous velocity gradients are less likely to appear.

In the homogeneous load experiment, the maps of velocity change show a similar behaviour as for DLT 1.3. The main shear zone is the bottom of the girder and the velocity decrease is bigger in these regions. When the load and the number of cracks increase, the velocity decrease becomes very strong and the fixed reference method becomes difficult to interpret. Nevertheless, at these loads, the girder is already severely damaged. Niederleithinger et al. (2018) have shown, using the stepwise method, that the gradient of velocity decrease from top to bottom for girder 1.5 can be better shown at higher loads using the stepwise method. For the load of 90 kN in 4.13(a), the fixed reference method shows an anomaly in the center of the area, where some big cracks appear on the outside. This anomaly is a fine damage indicator, which does not appear in the stepwise method. It shows that both methods are advantageous for different purposes. The question, which method to apply will be a task of pre-experimental evaluation. Nevertheless, a switch is still possible at later times, as the required data is the same.

CWI monitoring experiments of similar scale as the one presented here are rarely found in literature. Zhang et al. (2016) have investigated a 15-ton reinforced concrete beam (1.6 m × 6.1 m × 0.8 m) during a four-point loading experiment with CWI analysis. The specimen was not pre-stressed. For analysis they used the LOCADIFF location algorithm developed for crack detection using the sensitivity kernels of US measurements. With this technique they could provide a more detailed map of stress with good correlation to cracks found by visual inspection. Furthermore they found indications for the origin of micro-cracking in the specimen. With the possibility of a dense mapping of velocity changes using only a limited amount of source-receiver combinations, this method is an excellent tool for thorough data analysis. Nevertheless, the maps of velocity change created with the simple CWI analysis presented in this thesis have an acceptable resolution as well and provide a quick tool for almost real-time monitoring. Zones of increased stress caused by the loading were well mapped with this simple method as well. While it might not be suited for high level evaluation like crack density mapping, it is still showing good accordance with cracks and the fixed reference method even shows local perturbations, when cracks appear more or less isolated in a certain area.

5.3 Correlation of Velocity Change and Strain

The velocity change is linked to stress-strain changes by the acousto-elastic theory. The analysis of the relation of strain and velocity change seems to be linear for small loads. This fact can be used to illustrate strain changes in the specimen using embedded ultrasound sensors. A comparison of strain and velocity measurements at one or several points can be used as calibration. With a linear scaling it is then possible to create maps of strain change in the specimen. In this thesis, the main strain ϵ_1 is used (which is the maximum strain), calculated from strain measurement rosettes. The direction of the main stress and strain throughout the specimen is known for three-point loading experiments. The maps of strain created with the linear relation show a good fit to the theoretical strain distribution in a in such an experiment. Nevertheless, this relation only holds for small loads. This tool has been used in the aforementioned paper of Zhang et al. (2016) as well. As mentioned, their maps provide better resolution but the overall results show a similar and logical structure.

With increasing strain, the relation becomes non-linear. Acoustoelastic theory, as described in section 2.5.2, describes the relation of strain change and change of Young's modulus. Renaud et al. (2011) and Jin et al. (2017) show that the velocity change measured with high frequency US can be used to approximate the change in Young's modulus and to calculate the classical non-linear parameters with polynomial fitting.

With the measured strain in the girders and the ultrasonic measurements, this non-linear relation can be shown for loads up to 800 kN in DLT 1.3 and 110 kN in DLT 1.5, which is a phase where already numerous cracks have appeared. The values of β vary when changing the sensor type used for strain measurements, as the sensors recorded different values. As the inductive displacement sensor is an averaging measurement, I assume that the concrete strain gauge delivers more precise measurements, as it is a single point measurement.[1] Using the

[1]The US measurements are averaging over a larger area as well. The difference is that ϵ_1 might change its direction within the measured area in our experiment, while the velocity change is an undirected and relative quantity.

concrete strain gauges and velocity measurements directed in the direction of the main strain, the calculation at DLT 1.3 and DLT 1.5 produce the different β values as well. While the signs of the coefficients are the same, the results of DTL 1.5 are doubled compared to DLT 1.3. First of all, one must note that for DLT 1.5 the fits are not as good as for DLT 1.3. Especially in the first half the values scatter more. In figure 4.22 one can see that the velocity decrease varies a lot at similar strain levels. This means the velocity changed in the phases where the load remained constant. These delayed effects are called hysteresis and are described in the acoustoelastic theory in the non classical non-linear parameter alpha. This parameter is not evaluated in this thesis, as a precise determination would require precise small scale measurements. For a determination of hysteresis effects one needs a dense sampling after load change. In general, the repetition rate during those experiments was rather low looking at single sensor combinations. This is inevitable when monitoring with an array, as the sensors can not measure simultaneously, but have to measure one after another to avoid unwanted influence of scattered waves from distant measurements.

One can only speculate about the reasons why the hysteresis effects are stronger for girder 1.5. For sure it is linked to the difference in loading setup in general. The strain measurements in the single load experiment were done in an area less affected by the load, as it was not pressing on the specimen right above it. Therefore, secondary effects in this area might have a smaller influence, which explains the better fit of the data. This might also explain the different results of the polynomial fit. The measurements followed the trend for a longer time in DLT 1.3, as they were made in a less stressed area, while for DLT 1.5 the whole girder was loaded and the girder cracked early. In specimen 1.3, the strain level, which could be linked to velocity with the acoustoelastic theory, was almost 0.4 ‰ at the end of the non-linear relation. In DLT 1.5 it was only 0.12 ‰ (using the concrete strain gauges.) The velocity changes are also differing but by not by the same margin.

Another interesting aspect worth mentioning is that the measurements at DLT 1.5 show an increase in velocity right before the strain and velocity strongly decrease. This can be seen as an indicator before severe damage or even failure. This relation is an interesting aspect for future research.

Jin et al. (2017) have shown that β increases with increasing damage, as they repeated the measurements at the same specimen with different damage levels. In this experiment, only one damage state can be used, as the load was stepwise increased and the specimen was never completely unloaded after the start of the experiment. In the experiment in Jin et al. (2017), the maximum parameter β was -54, corresponding to the strongest damage level they experimented with. This value is in good agreement with the values from DLT 1.3. Unfortunately, the cubic parameter δ has a different sign in our experiment and the magnitude differs as well for two of the four presented results (10^6 in Jin et al. (2017)). The experiments in this thesis were done with higher strain levels, which could cause the difference, as δ becomes more dominant with bigger strains. It is noted in Jin et al. (2017) that the results should in theory be corrected for Poison effects, but as the measurements were all conducted in the same material, they renounce correction for this effect. The given values in this thesis are also not corrected for the Poison effect, so they can be compared with the values from the mentioned publication.

According to Renaud et al. (2011) the third parameter in the polynomial fit quantifies an offset when the material is in an nonequilibrium state, excited by low frequencies. As this

parameter is small for all four displayed calculations, this effect is not occurring in the analysed measurement. This is expected, as high frequencies were used.

In other publications (e.g Payan et al. (2010)), the non-linear parameter β was calculated for concrete with the help of Murnaghan's third-order constants. For this calculation, different wave polarizations are required. Payan et al. (2010) calculate a beta value of -151 for concrete. This value is in the range of the experiment with the concrete strain gauge at DLT 1.5, as well as in the range of the results at the inductive displacement sensors in DLT 1.3. Therefore, the general quality of the strain measurements has to be questioned. In the experiments used for comparison, the strain was always estimated with the relative length changes on the outside of the small specimen. This is not possible for larger experiments, as the strains will vary throughout the specimen. In general, it is difficult to compare the results of Payan et al. (2010) to this thesis, as two different techniques were used, but the strong variations comparing the different papers show that the variations in this thesis might simply be explained by the different experimental structure. Sensor position, stress in the sensed area and the way the load is applied are factors possibly influencing the results. For an extended analysis, future experiments are needed.

If it can be shown that the parameter changes with increasing damage, the magnitude is not crucial for damage assessment, but rather the trend of β. In this thesis, I could not show that β increases with damage, but I could show that the calculated value is of similar size than for a damaged specimen using similar methods.

For monitoring, a comparison of β values at different times is necessary. When the ultrasound transducers are embedded, from time to time small measurement campaigns with non destructive loading can deliver the required data for the assessment of the evolution of the non-linear parameter over time.

The fact that the relation between strain and velocity change can be mathematically approximated and expressed for higher loads beyond the linear relation shows a direct link of CWI velocity change and strain even if the specimen starts to crack. This shows that monitoring in a partially cracked medium is still possible using non-linear parameters, as long as the specimen is not completely destroyed.

Chapter 6

Summary and Outlook

The goal of this thesis was the analysis of ultrasonic measurements in concrete bridge girders. These girders were loaded until failure in point load and homogeneous load experiments. Ultrasonic measurements were conducted throughout the loading. The application of US measurements (60 kHz) as a monitoring technique requires the extraction of damage sensitive parameters.

The first parameter analysed using the US measurements is the diffusivity. Diffusivity describes how fast energy spreads through a medium. It is calculated with a linear fit to the energy of the recorded signal, using a strong simplification of the girder geometry. Cracks in the concrete will increase scattering and the diffusivity should decrease. This bears potential for a possible damage indicator. Indeed, the results show that the diffusivity decreases when the load is increased. Furthermore, an increase in pre-stress, which closed existing cracks resulted in an increase of diffusivity. Unfortunately, the calculated values differ using different source-receiver combinations. Especially for large source-receiver offset, the application of the diffusive approximation shows some shortcomings. Nevertheless, a comparison of the values of a majority of sensor combinations with literature values shows that the results are within reasonable range.

The diffusivity is of special importance for modelling and inversion, which is not applied in this thesis. As a frequency and material dependant parameter it can be calculated for undamaged concrete using a calibration specimen with the same concrete used for construction. Therefore, before setting up a monitoring array, the diffusivity can be calculated for the used transducers and concrete and can be used in the following US analysis.

In a next step, the ultrasound velocity change during the loading experiments was calculated. The method used, coda wave interferometry (stretching method), requires a selection of the time window for correlation of a signal reference. It is shown that the stretching method is pretty robust to changes in the time window. The only requirement is the inclusion of reasonably much signal energy and the avoidance of pure noise. With the time window defined, the velocity changes are calculated. For both types of loading experiments, the velocity change shows a good agreement with the expected stresses and strains, as well as

with the recorded cracking patterns. The two different approaches to the stretching method using a fixed reference signal and a stepwise changing reference signal both deliver comparable results in the early loading phase. As soon as the specimens are severely damaged, the fixed reference method delivers results difficult to interpret, while the stepwise method still works well. On the contrary, the fixed reference method shows steeper gradients locally when the material changes and cracks appear, while the fixed reference sometimes does not show these changes. Therefore, local damage indicators might be detected better using the fixed reference method.

As for monitoring tasks the load on the specimen will not be as high as in the end of this experiment. Both methods can be used with similar results and the velocity change is a well suited parameter for damage detection.

A comparison of the CWI results from this thesis with inversion results (LOCADIFF) of an experiment of similar size shows, that the resolution in the maps of velocity (and therefore strain) changes increases when inversion is applied. Nevertheless, both methods map stressed areas in the specimen. Therefore, for monitoring a simple application of CWI is sufficient.

Using strain measurements in parts of the specimen, the relation of strain and velocity change was investigated. In early stage of loading the relation is linear. This way, the calculated velocity changes in the early loading phase can be directly linked to the strain in a specimen. This is a nice tool for presentation of results for a monitoring center, as engineers might be more familiar with strain than velocity changes. As soon as the load increases, the relation becomes non-linear. Acousto-elastic theory describes this relation. The change of velocity with increasing strain can be fitted with a second order polynomial describing the evaluation of the velocity change. The parameters from the fitting process are the classical non-linear parameters β and δ. The calculated beta value is differs comparing the investigated girders. The values are within the range of literature values. As literature values and the values in this thesis vary, the measurements of strain in those experiments might have a strong influence. The results using different techniques seem to vary strongly. A dependence of β on the damage level in the specimen can not be investigated with this experiment. As literature suggests that beta is indeed sensitive to the damage level, several repeated loading experiments at different damage levels would be required for further analysis. Still, showing that the relation between velocity change and strain is predictable up to some point in a loading experiment indicates the potential of the extracted parameters for the assessment of the quality of a structure. The second parameter δ could not be evaluated in comparison to other studies, as they investigated the relation at smaller strain levels. As δ becomes more influential with increasing strain, a comparison would not have been meaningful.

In the scope of permanent bridge monitoring, I believe that the velocity analysis with ultrasound has the highest potential, as it is a simple and fast method. The diffusivity in this large scale experiment has shown rather unstable behaviour and did not deliver additional information as a direct damage indicator. Nevertheless, it is required for modelling and inversion, which have a big potential in concrete monitoring. It should be evaluated for the used concrete and sensors, as it provides additional information on the scattering parameters. The non-linear parameters are reported to be damage sensitive in literature. The given experiment was not suited for evaluation of the influence of damage on those parameters, but it was shown that one can simply calculate them with a combination of strain measurements and ultrasound measurements. Therefore, these parameters bear potential for monitoring, as long

as the setup makes an evaluation possible. A crucial factor for such analysis is the repetition rate of ultrasound measurements. A dense sampling is required to evaluate the variations in strain. This is difficult in an array structure, as the measurements have to be done one after another for different source-receiver combinations. For the evaluation of the velocity-strain relation a high repetition rate at a single point is required.

The data used from the described experiment is a valuable tool for evaluating US analysis. In this thesis only two out of five measurement campaigns were investigated, so there is plenty of data available for future investigation. It is a good database for training and studying, as the data is of good quality and an extensive evaluation is already available. In some points, the size of the experiment with its practical limitations caused some problems in several steps of data analysis, but in general the small scale laboratory experiments can be applied to an experiment of larger scale like the one conducted at RWTH Aachen.

By and large, monitoring of bridges with ultrasound already offers tools well understood and documented. With the addition of some of the parameters described in this thesis, a monitoring strategy can be developed. However, this is a task for upcoming studies, as the incorporated parameters need further analysis and testing in separate experiments.

Bibliography

Aki, K. (1969). Analysis of the Seismic Coda of Local Earthquakes as Scattered Waves. *Journal of Geophysical Research*, 74(2):615–631. doi: 10.1029/JB074i002p00615.

Chandrasekhar, S. (1960). *Radiative Transfer*. Dover Books on Intermediate and Advanced Mathematics. Dover, New York.

Chen, J., Jayapalan, A. R., Kim, J.-Y., Kurtis, K. E., and Jacobs, L. J. (2010). Rapid Evaluation of Alkali-Silica Reactivity of Aggregates Using a Nonlinear Resonance Spectroscopy Technique. *Cement and Concrete Research*, 40(6):914–923. doi: 10.1016/j.cemconres.2010.01.003.

Dankert, J. and Dankert, H. (2013). *Technische Mechanik: Statik, Festigkeitslehre, Kinematik/Kinetik*. Springer-Verlag.

Deroo, F. (2009). Damage Detection in Concrete Using Diffusive Ultrasound Measurements and an Effective Medium Theory for Wave Propagation in Multi-Phase Materials. Master's thesis, Georgia Institute of Thechnology.

Deroo, F., Kim, J.-Y., Qu, J., Sabra, K., and Jacobs, L. J. (2010). Detection of Damage in Concrete Using Diffuse Ultrasound. *The Journal of the Acoustical Society of America*, 127(6):3315–3318. doi: 10.1121/1.3409480.

Fröjd, P. (2018). *Structural Health Monitoring of Concrete Structures Using Diffuse Waves*. PhD thesis, Lund University.

Fröjd, P. and Ulriksen, P. (2017). Frequency Selection for Coda Wave Interferometry in Concrete Structures. *Ultrasonics*, 80:1–8. doi: 10.1016/j.ultras.2017.04.012.

Gould, P. L. and Feng, Y. (1994). *Introduction to Linear Elasticity*. Springer.

Ishimaru, A. (1978). *Wave Propagation and Scattering in Random Media*. Academ. Press.

Jin, J., Moreno, M. G., Riviere, J., and Shokouhi, P. (2017). Impact-Based Nonlinear Acoustic Testing for Characterizing Distributed Damage in Concrete. *Journal of Nondestructive Evaluation*, 36(3):51. doi: 10.1007/s10921-017-0428-2.

Kamada, T., Nagataki, S., and Iwanami, M. (1997). Evaluation of Material Deterioration in Concrete by Nondestructive Testing Methods. In *International Conference on Engineering Materials, Ottawa, CA*, pages 453–466.

Larose, E., Planes, T., Rossetto, V., and Margerin, L. (2010). Locating a Small Change in a Multiple Scattering Environment. *Applied Physics Letters*, 96(20):204101. doi: 10.1063/1.3431269.

Lobkis, O. I. and Weaver, R. L. (2003). Coda-Wave Interferometry in Finite Solids: Recovery of P-to-S Conversion Rates in an Elastodynamic Billiard. *Physical review letters*, 90(25):254302. doi: 10.1103/PhysRevLett.90.254302.

Murnaghan, F. D. (1937). Finite Deformations of an Elastic Solid. *American Journal of Mathematics*, 59(2):235–260. doi: 10.2307/2371405.

Neroth, G. (2011). *Wendehorst Baustoffkunde*, volume 27. Vieweg + Teubner.

Niederleithinger, E. (2018). Querkrafttragfähigkeit von Spannbetonträbrücken. Technical report, Bundesamt für Materialforschung und -prüfung.

Niederleithinger, E., Wang, X., Herbrand, M., and Mller, M. (2018). Processing Ultrasonic Data by Coda Wave Interferometry to Monitor Load Tests of Concrete Beams. *Sensors*, 18(6). doi: 10.3390/s18061971.

Niederleithinger, E., Wolf, J., Mielentz, F., Wiggenhauser, H., and Pirskawetz, S. (2015). Embedded Ultrasonic Transducers for Active and Passive Concrete Monitoring. *Sensors*, 15(5):9756–9772. doi: 10.3390/s150509756.

Pacheco, C. and Snieder, R. (2005). Time-Lapse Travel Time Change of Multiply Scattered Acoustic Waves. *The Journal of the Acoustical Society of America*, 118(3):1300–1310.

Payan, C., Garnier, V., and Moysan, J. (2010). Potential of Nonlinear Ultrasonic Indicators for Nondestructive Testing of Concrete. *Advances in Civil Engineering*, 2010.

Planès, T. and Larose, E. (2013). A Review of Ultrasonic Coda Wave Interferometry in Concrete. *Cement and Concrete Research*, 53:248–255. doi: 10.1016/j.cemconres.2013.07.009.

Ramamoorthy, S. K., Kane, Y., and Turner, J. A. (2004). Ultrasound Diffusion for Crack Depth Determination in Concrete. *The Journal of the Acoustical Society of America*, 115(2):523–529. doi: 10.1121/1.1642625.

Renaud, G., Talmant, M., Callé, S., Defontaine, M., and Laugier, P. (2011). Nonlinear Elastodynamics in Micro-Inhomogeneous Solids Observed by Head-Wave Based Dynamic Acoustoelastic Testing. *The Journal of the Acoustical Society of America*, 130(6):3583–3589. doi: 10.1121/1.3652871.

Rossetto, V., Margerin, L., Planes, T., and Larose, E. (2011). Locating a Weak Change Using Diffuse Waves: Theoretical Approach and Inversion Procedure. *Journal of Applied Physics*, 109(3):034903. doi: 10.1063/1.3544503.

Sens-Schönfelder, C. and Wegler, U. (2006). Passive Image Interferometry and Seasonal Variations of Seismic Velocities at Merapi Volcano, Indonesia. *Geophysical research letters*, 33(21). doi: 10.1029/2006GL027797.

Sheng, P. (1995). *Introduction to Wave Scattering, Localization, and Mesoscopic Phenomena*. Elsevier.

Sheriff, R. E. (2002). *Encyclopedic Dictionary of Applied Geophysics*. Society of exploration geophysicists.

Snieder, R., Grêt, A., Douma, H., and Scales, J. (2002). Coda Wave Interferometry for Estimating Nonlinear Behavior in Seismic Velocity. *Science*, 295(5563):2253–2255. doi: 10.1126/science.1070015.

Stähler, S. C., Sens-Schönfelder, C., and Niederleithinger, E. (2011). Monitoring Stress Changes in a Concrete Bridge with Coda Wave Interferometry. *The Journal of the Acoustical Society of America*, 129(4):1945–1952. doi: 10.1155/2010/238472.

Stehly, L., Campillo, M., Froment, B., and Weaver, R. L. (2008). Reconstructing Green's Function by Correlation of the Coda of the Correlation (c3) of Ambient Seismic Noise. *Journal of Geophysical Research: Solid Earth*, 113(B11). doi: 10.1029/2008JB005693.

Toupin, R. and Bernstein, B. (1961). Sound Waves in Deformed Perfectly Elastic Materials. Acoustoelastic Effect. *The Journal of the Acoustical Society of America*, 33(2):216–225. doi: 10.1121/1.1908623.

Wapenaar, C. (1989). *Elastic Wave Field Extrapolation - Redatuming of Single and Multi-Component Seismic Data*, volume 2. Elsevier Science, 1 edition.

Weaver, R. (1998). Ultrasonics in an Aluminum Foam. *Ultrasonics*, 36(1-5):435–442. doi: 10.1016/s0041-624x(97)00064-4.

Yilmaz, Ö. (2001). *Seismic Data Analysis: Processing, Inversion, and Interpretation of Seismic Data*. Society of exploration geophysicists.

Zhang, Y., Planes, T., Larose, E., Obermann, A., Rospars, C., and Moreau, G. (2016). Diffuse Ultrasound Monitoring of Stress and Damage Development on a 15-ton Concrete Beam. *The Journal of the Acoustical Society of America*, 139(4):1691–1701. doi: doi.org/10.1121/1.4945097.

Zilch, K. and Zehetmaier, G. (2006). *Bemessung im Konstruktiven Betonbau: Grundlagen und Tragfähigkeit*. Springer-Verlag.

Appendix A

Appendix

A.1 Matlab Code

In the following, some matlab codes are appended used for different tasks in this thesis to illustrate the methods used. The code used for CWI calculation is a modified version of code created by Ernst Niederleithinger and will therefore not be appended to this thesis. The main parts of this file are dealing with extraction of the measurement data from the corresponding data files, as well as preprocessing. The CWI analysis is using the trapezoid rule for integration.

A.1.1 Random Walk

In the theory chapter US propagation is compared to a random walk. The following code is calculating a rudimentary random walk on a grid with receivers counting how often the random walker visited their positions. When a scattering event occurs, the signal is attenuated stronger. An approach for a more sophisticated simulation could include diffusivity values for example.

```
%% Rudimentary random walk

clear all

rng shuffle

%% transition Probability Matrix -> too much storage for bigger than 100x100 grid -> sparse indexing
    ?
%
% % grid size 100*100
% tic
% gs = 1000;
% n = gs^2;
%
% Pg = sparse(n,n);
%
% for i = 1:n-1
%     Pg(i,i+1) = 1/8;
%     Pg(i+1,i) = 1/8;
%     Pg(i,i+gs-1) = 1/8;
%     Pg(i,i+gs) = 1/8;
%     Pg(i,i+gs+1) = 1/8;
%     Pg(i+gs-1,i) = 1/8;
```

```
%     Pg(i+gs,i) = 1/8;
%     Pg(i+gs+1,i) = 1/8;
% end
% toc
% Pg = sparse(Pg(1:n,1:n));

%% Simple approach:

% Source and receiver position position:
PS = [0 0];
PR1 = [-10 0];
PR2 = [0 -10];
PR3 = [0 10];
PR4 = [10 0];

% init values:
damp = 0.0002; %damping factor after every timestep
damps = 0.003; %damping factor when scattered
ns = 500; %number of timesteps
nwalk = 100000; %number of random walks
pscatter = 0.8; %scattering probability

% domain Boundaries:
xboundr = 100;
yboundr = 100;
xboundl = -100;
yboundl = -100;

% initiate values:
SigR1 = zeros(1,ns);
SigR2 = zeros(1,ns);
SigR3 = zeros(1,ns);
SigR4 = zeros(1,ns);
movexPrev = 0;
moveyPrev = 0;

tic
for k = 1:nwalk

xmove = randi([-1,1]);
ymove = randi([-1,1]);
P = zeros(ns,2);
P(1,:) = PS;
signStr = 1;

for ii = 1:ns-1


% evaluate if receiver records something

if P(ii,1) == PR1(1) && P(ii,2) == PR1(2)
    SigR1(ii) = SigR1(ii)+signStr;
end

if P(ii,1) == PR2(1) && P(ii,2) == PR2(2)
    SigR2(ii) = SigR2(ii)+signStr;
end

if P(ii,1) == PR3(1) && P(ii,2) == PR3(2)
    SigR3(ii) = SigR3(ii)+signStr;
end

if P(ii,1) == PR4(1) && P(ii,2) == PR4(2)
    SigR4(ii) = SigR4(ii)+signStr;
end

% next step direction and boundary reflection

if P(ii,1) >= xboundr
    xmove = -1;
    ymove = ymove;
elseif P(ii,1) <= xboundl
    xmove = 1;
    ymove = ymove;
elseif P(ii,2) >= yboundr
    xmove = xmove;
    ymove = -1;
elseif P(ii,2) <= yboundl
    xmove = xmove;
    ymove = 1;
else
    changedir = randi([0,100])/100;
    if changedir <= pscatter
    xmove = randi([-1,1]);
    ymove = randi([-1,1]);
    end
end

% step to next coordinate
```

```
P(ii+1,1) = P(ii,1) + xmove;
P(ii+1,2) = P(ii,2) + ymove;

% signal strength attenuation:                                          116

if movexPrev == xmove && moveyPrev == ymove %If not scattered
    signStr = (signStr*exp(-damp*ii))*(-1);
else                                        %If scattered
    signStr = (signStr*exp(-damps*ii))*(-1);                            121
end
end
end
toc
```

A.1.2 Diffusivity

The calculation of diffusivity and dissipation rate is a done with the solution of the linear system of equation described in section 2.3.4. For the calculation of the spectral energy density a function called EPS.m was written.

Main file:

```
load('Signal.mat');
                                                                        3
%% Energy power spectrum input:
d = 2; % dimensions
freqband = [5000 115000];
l_window = 100;
overlap = 0.9;                                                          8
dt = 1/samplefreq; %saved in Signal.mat

%source receiver coordinates:
sx = 1.27;
sy = 0.405;                                                             13
sz = 0.0;

rx = 1.765;
ry = 0.4;
rz = 0.0;                                                               18

r = sqrt((rx-sx)^2+(ry-sy)^2+(rz-sz)^2);

%% Calculate the spectral energy denisty:
                                                                        23
[E,t] = EPS(signal,samplefreq,l_window,overlap,freqband);

%% RHS of equation

B(ii,:) = log(E)+d/2*log(t);                                            28

%% linear model

% find starting point above a certain noise level:
start = find(B>-8.5,1);                                                 33
t_used = t(start:250);

% initialize matrix for linear system:
A = ones(length(t_used),3);
A(:,2) = t_used;                                                        38
A(:,3) = 1./t_used;

%solve the linear sytem
x = A\B(ii,start:250)';
                                                                        43
%% Extraction of desired parameters:
D = -(r^2)/(4*x(3));
sigma = -x(2);
```

EPS.m:

```
function [E_dens,d] = EPS(signal,samplefreq,l_window,overlap,freqband)
%% Energy power spectrum calculation
% Input:
% signal: singal as time series                                         4
% samplefreq = samplefrequency in Hz
```

```
% l_window = window length in samples
% overlap of windows between 0 and 1;
% frequency band used around f_c of length df (2 component vectore)

%% Test parameters:
% dt = 1/samplefreq;
% overlap = 0.9;
% l_window = 100; %samples

%% calculate the number of overlapping samples:
noverlap = overlap * l_window;


%% calculate the spectrogram which gives the power spectral energy density ps
[s,f,d,ps] = spectrogram(signal,l_window,noverlap,[],samplefreq);
%spectrogram(signal,l_window,noverlap,[],samplefreq)


%% Find the upper and lower frequency boundary used for energy calulation
lower = find(f>=freqband(1),1);
upper = find(f>=freqband(2),1);

range = ps(lower:upper,:);

%% Calculate the spectral energy density (integration over each collumn):
E_dens = trapz(range);

% plot(d,log(E))
```

A.1.3 Correlation of Velocity and Strain

The second polynomial fit is done with the matlab function polyfit. The following code shows is an example for DLT 1.3.

```
%% extract non linear constants from depsilon and dv
%% Load data
load('deflection_DLT1_3.mat') % Load
load('t.mat') % time of strain measurements
load('Hauptspannungen.mat') % Main strains

tnum = datenum(t); % convert time format


%% Sensor combinations:
%% conc:
% sens1 = 'S08E09'
% sens2 = 'S09E10'

sens1 = 'S03E09'
sens2 = 'S09E15'
%
% sens1 = 'S04E09'
% sens2 = 'S09E14'

%% WA3:
% sens3 = 'S07E19'
% sens4 = 'S07E08'
%
sens3 = 'S07E18'
sens4 = 'S07E13'
% %
% sens3 = 'S02E07'
% sens4 = 'S07E20'

%% WA4:
sens5 = 'S10E11'

%% Load CWI data:

%Fixed refference:
US1 = load([sens1 '/' sens1 '-20161117-belastung-cwiresults-e.mat']);
US2 = load([sens2 '/' sens2 '-20161117-belastung-cwiresults-e.mat']);
US3 = load([sens3 '/' sens3 '-20161117-belastung-cwiresults-e.mat']);
US4 = load([sens4 '/' sens4 '-20161117-belastung-cwiresults-e.mat']);
US5 = load([sens5 '/' sens5 '-20161117-belastung-cwiresults-e.mat']);

% Step CWI:
% US1 = load([sens1 '/' sens1 '-20161117-stepcwiresults']);
% US2 = load([sens2 '/' sens2 '-20161117-stepcwiresults']);
% US3 = load([sens3 '/' sens3 '-20161117-stepcwiresults']);
% US4 = load([sens4 '/' sens4 '-20161117-stepcwiresults']);
% US5 = load([sens5 '/' sens5 '-20161117-stepcwiresults']);

%% Interpolate the US measurement to the same measurement time for calculation of the mean velocity
    change:
US2.bestv_interp = interp1(US2.zeitnum'+(1:length(US2.zeitnum))*1E-9,US2.bestv,US1.zeitnum);
```

```
US4.bestv_interp = interp1(US4.zeitnum'+(1:length(US2.zeitnum))*1E-9,US4.bestv,US3.zeitnum);US5.
    bestv_interp = interp1(US5.zeitnum'+(1:length(US2.zeitnum))*1E-9,US5.bestv,US1.zeitnum);

% US2.bestv_interp = interp1(US2.zeitnum(1:end),US2.cumbestv(1:end),US1.zeitnum(1:end));
% US4.bestv_interp = interp1(US4.zeitnum(1:end),US4.cumbestv(1:end),US1.zeitnum(1:end));

%% Calculation of the velocity change as a mean between two measurements:
mean_bestv = 1/2*(US1.bestv+US2.bestv_interp');
mean_bestv(isnan(mean_bestv)) = 0; % avoid possible NAN values
mean_bestv2 = 1/2*(US3.bestv+US4.bestv_interp');
mean_bestv2(isnan(mean_bestv2)) = 0;
mean_bestv3 = US5.bestv(1:end);
mean_bestv3(isnan(mean_bestv3)) = 0;

% mean_bestv = 1/2*(US1.cumbestv(1:end)+US2.bestv_interp');
% mean_bestv2 = 1/2*(US3.bestv(1:end)+US4.bestv_interp');
% mean_bestv3 = US5.bestv(1:end);

%% curve fitting

% conc DMS:
samplerange = (1:32); %Used datapoints

eps1_conc = eps_1_conc/1000; %Strain data converted to [m/m]
eps2_conc = eps_2_conc/1000;

% extract strain values at US measurement times:
eps_short = interp1(tnum,eps1_conc(1:length(tnum)),US1.zeitnum);
eps_short(isnan(eps_short)) = 0;
eps1_conc = eps_short';
% adapt velocity change for fit
v1 = -2*mean_bestv;

% Fit and evaluation of polynom
fit = polyfit(eps1_conc(samplerange),v1(samplerange),2);
f = polyval(fit,eps1_conc(samplerange));

% Plot
figure(1)
plot(eps1_conc(samplerange)*1000,f*100,'LineWidth',1) % scaled to % and
hold on
scatter(eps1_conc(samplerange)*1000,v1(samplerange)*100,'LineWidth',1)
xlabel('Strain [   ]','FontSize',14)
ylabel('2 * CWI velocity change [%]','FontSize',14)
title('D4 - up to 800 kN load', 'FontSize',14)
leg = legend('Fitting', 'Data');
leg.FontSize = 14;
ann = annotation('textbox',[0.15 0.1 0.3 0.1],'String', ['2\Deltav/v = ' num2str(fit(1),'%10.1e') '\
    epsilon^2 - ' num2str(abs(round(fit(2)))) '\epsilon - ' num2str(abs(fit(3)),'%10.1e')],'
    FitBoxToText','on');
ann.FontSize = 14;

% Wa 3:
samplerange = (1:27);

eps1_WA3 = eps_1_WA3/1000;
eps2_WA3 = eps_2_WA3/1000;

eps_short = interp1(tnum,eps1_WA3(1:length(tnum)),US3.zeitnum);
eps_short(isnan(eps_short)) = 0;
eps1_WA3 = eps_short';
v2 = -2*mean_bestv2;

fit = polyfit(eps1_WA3(samplerange), v2(samplerange),2);
f = polyval(fit,eps1_WA3(samplerange));

figure(2)
plot(eps1_WA3(samplerange)*1000, f*100, 'LineWidth',1)
hold on
scatter(eps1_WA3(samplerange)*1000,v2(samplerange)*100,'LineWidth',.5)
xlabel('Strain [   ]','FontSize',14)
ylabel('2 * CWI velocity change [%]','FontSize',14)
title('R3 - up to 700 kN load', 'FontSize',14)
leg = legend('Fitting', 'Data');
leg.FontSize = 14;
ann = annotation('textbox',[0.15 0.1 0.3 0.1],'String', ['2\Deltav/v = ' num2str(fit(1),'%10.1e') '\
    epsilon^2 - ' num2str(abs(round(fit(2)))) '\epsilon - ' num2str(abs(fit(3)),'%10.1e')],'
    FitBoxToText','on');
ann.FontSize = 14;
```